polymer papers

Simulation of large strain plastic deformation and texture evolution in high density polyethylene

B. J. Lee†, A. S. Argon‡, D. M. Parks, S. Ahzi† and Z. Bartczak*§
*Departments of Mechanical Engineering and *Chemical Engineering, Massachusetts Institute of Technology, Cambridge, MA 02139, USA*
(Received 19 February 1993)

A micromechanically based composite model which we have recently proposed is employed to study large plastic deformation and texture evolution in initially isotropic high density polyethylene (HDPE) under different modes of straining. Attention is focused on the macroscopic stress–strain response and the evolution of crystallographic, morphological and macromolecular textures in HDPE subject to uniaxial tension and compression, simple shear and plane strain compression. Comparison of the predicted results with experimental observations (e.g. stress–strain measurements, wide-angle X-ray scattering and small-angle X-ray scattering studies of deformed material) shows excellent agreement in nearly all respects.

(Keywords: plastic deformation; texture evolution; high density polyethylene)

INTRODUCTION

Many polymers can undergo large plastic deformation resulting in high anisotropy due to preferential orientation (texturing) of macromolecules and morphology. This is particularly true for semicrystalline polymers, which can be processed into fibres and ribbons with very attractive mechanical properties. Plastic deformation of semicrystalline polymers, in particular polyethylene, has been studied intensively by experiment from the viewpoint of changes in morphology as well as characterization of mechanisms of deformation and their relative resistances[1–11]. The principal mechanisms involved in the plastic deformation of semicrystalline polymers are crystallographic in nature, albeit very complex when considered in the context of the local morphology. The specific mechanisms involved in plastic deformation of semicrystalline polymers have been reviewed by many investigators; among those, the reviews by Bowden and Young[4] and by Haudin[5] are noteworthy. Many of these investigations of the mechanisms of deformation have been concerned with high density polyethylene (HDPE) because of its relatively simple structure and its high degree of crystallinity. The plastic deformation mechanisms of highly textured HDPE prepared by plane strain compression in a channel-die as a convenient approximation in bulk to a single crystalline material were studied recently in great detail by Bartczak *et al.*[6]. The deformation processes of HDPE were investigated in a wide variety of loading conditions such as uniaxial tension[7], uniaxial compression[8], simple shear[9,10] and plane strain compression[11]. On the other hand, there have been relatively few studies aimed at the numerical simulation of large plastic deformation and texture evolution in semicrystalline polymers, in a mechanistically faithful manner.

The morphology of undeformed semicrystalline polymers, when melt crystallized, is often spherulitic[12,13]. A spherulite consists of a radial arrangement of broad thin crystalline lamellae separated by amorphous layers. This mesostructural unit is shown schematically in *Figure 1a*. The numerous studies of plastic straining of semicrystalline polymers in extensional flow have now established that important morphological reorganization occurs as a result of the deformation, with the structure changing from spherulitic to a highly oriented one

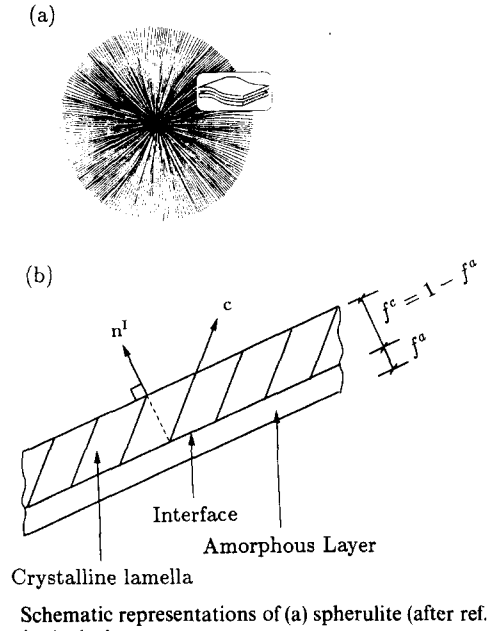

Figure 1 Schematic representations of (a) spherulite (after ref. 13) and (b) composite inclusion

† Present address: Department of Applied Mechanics and Engineering Sciences, University of California, San Diego, La Jolla, CA 92093, USA
‡ To whom correspondence should be addressed
§ Present address: Centre of Molecular and Macromolecular Studies, Polish Academy of Sciences, Sienkiewicza 112, 90-363 Lodz, Poland

0032-3861/93/173555-21

consisting of alternating crystalline and amorphous layers. At the same time, crystallographic axes of the crystalline lamellae and macromolecular chains of the amorphous component rotate and tend to align preferentially with respect to principal axes of macroscopic deformation. Thus it has been established that, when plastically deformed, semicrystalline polymers develop three important types of texture: (1) a *crystallographic texture*, due to preferential orientation of crystallographic axes in the crystalline lamellae; (2) a *morphological texture*, due to preferential orientation of the normals to the broad lamellar faces; and (3) a *macromolecular texture* in the amorphous phase, promoted by molecular alignment with the direction of maximum stretch. The evolution of texture with large plastic deformation strongly affects the macroscopic mechanical behaviour of semicrystalline polymers. For instance, a strong textural hardening is observed in tension but not in simple shear of HDPE[7,9,10].

We have developed a micromechanically based model of large plastic deformation in semicrystalline polymers to predict both the evolution of textural anisotropy and macroscopic mechanical behaviour under different modes of straining[14]. The aim of this paper is to report the progress we have made in developing the model and illustrating its applicability by comparing numerical predictions with a wide variety of experimental observations. In our viscoplastic composite model, we neglect elasticity and pressure sensitivity of deformation resistance, but account for the mechanically coupled response of both crystalline and amorphous phases in contributing to large plastic deformation. Constitutive models of plastic deformation in each phase are based on well-established microstructural mechanisms and their relative resistances. An aggregate of two-phase composite inclusions, each consisting of a crystalline lamella attached to its corresponding amorphous layer, as shown schematically in *Figure 1b*, is used to model semicrystalline polymers. This composite inclusion constitutes the basic structural element of the semicrystalline polymer — whether in spherulitic or in the eventual highly aligned morphology. Each of the two components of the composite inclusion is assumed to deform homogeneously. Moreover, crystalline/amorphous interface compatibility and equilibrium are satisfied throughout the entire deformation history. In the proposed model, a so-called Sachs-like aggregate interaction law is employed to relate the volume-average deformation and stress of a composite inclusion to the respective macroscopic fields, in preference to a so-called Taylor-like interaction law.

HDPE was chosen as a model material for the present study because of the large amount of existing experimental data and relatively high degree of understanding of the plastic deformation mechanisms for this material. However, the operational procedures developed are equally well adaptable to other semicrystalline polymers with different crystal structures, with glassy amorphous phases, or both. Undeformed HDPE has a spherulitic morphology with spherical packing of crystalline lamellae separated by layers of amorphous phases. The thickness of the lamellar inclusions ranges from 50 to 250 Å, and the lateral dimensions range from 1 to 50 μm. HDPE crystals have an orthorhombic structure. At room temperature, the amorphous phase of HDPE is in the rubbery regime[15]. The crystalline phase of HDPE can deform plastically by crystallographic slip, twinning and stress-induced martensitic transformations. However, each of these mechanisms leaves the material direction parallel to the crystallographic chain direction inextensible, so they provide fewer than the five independent deformation modes required to accommodate arbitrary plastic deformation[3,4]. Plastic deformation of the crystalline phase is in general accompanied by deformation of the amorphous phase. In the absence of cavitation, the amorphous phase deforms primarily by interlamellar shear[8,10,11]. While interlamellar separation has also been suggested[16,17], we do not consider that here as an acceptable mode for bulk deformation without cavitation. We note, however, that in cases where the initial angle between the chain direction and the lamellar normal is not zero, and the lamella can thicken by chain slip, a small amount of kinematically linked thickening of the amorphous layer is then possible. This will result in a small amount of interlamellar separation which is routinely taken into consideration in our model. The simultaneous activity of several deformation mechanisms allows the initial structure to be transformed in a continuous manner to any and all of the final oriented states. Thus, we consider the often observed transitional cavitational processes (micronecking, etc.) not as fundamental, but as inessential artifacts of tensile deformation. We have used the newly developed composite model to simulate stress–strain response and texture evolution during deformation of HDPE to large plastic strain under several different modes of straining. Predicted results are compared to experimental observations of earlier investigations as well as our own more recent results reported in greater detail elsewhere[6,8,10,11].

Operational notation used in this paper is based on the following conventions. Scalars are given in italics (A, a, α), vectors are lower case bold-face ($\mathbf{a}$) and second-order tensors are upper case bold-face ($\mathbf{A}$). The superscripts I, c and a designate inclusion, crystalline lamella and amorphous layer, respectively. When required, repeated Cartesian subscripts are summed from 1 to 3. Greek subscripts range from 1 to 2.

MODEL DESCRIPTION

Basic assumptions

To model large strain plastic deformation and texture evolution in semicrystalline polymers, we neglect elasticity and account for intrinsic non-linear viscoplastic behaviour of both crystalline and amorphous phases. The decision to neglect elasticity is motivated both by the increased simplicity of the constitutive modelling and by the argument that at very large strains, elasticity neither contributes significantly to overall deformation nor has much effect on the development of texture. Incompressibility is assumed in both phases. We assume that the basic element constituting semicrystalline polymers is a two-phase composite inclusion represented by a crystalline lamella and its associated amorphous layer. Due to their large aspect ratio, the composite inclusions are modelled as infinitely extended 'sandwiches' with a planar crystalline/amorphous interface (*Figure 1b*). Each composite inclusion is characterized by its interface normal, $\mathbf{n}^{\mathrm{I}}$, and the relative thicknesses f^{a} and f^{c} $(=1-f^{\mathrm{a}})$ of the amorphous and crystalline phases, respectively. The relative thickness f^{a} also represents the inclusion

volume fraction of the amorphous phase, which is assumed to be constant and identical for all inclusions. Furthermore, each composite inclusion is presumed to have equal volume and initial thickness. Parenthetically, we note that one of our associated recent experimental studies[11] demonstrates conclusively that, under certain circumstances, the interface between the crystalline and amorphous phases can translate during morphological restructuring purely in response to reduction of interfacial free energy. These effects are not incorporated into our model, with certain consequences on our predictions which we will point out. We assume that the material interface between the two components of the inclusion remains distinct throughout and does not migrate. In the following, we will discuss the constitutive models for crystalline and amorphous phases of the HDPE and the behaviour of the composite inclusion. Then, the local interaction law and solution procedure for the proposed composite model will be discussed briefly. We then apply the model to predict stress–strain behaviour and texture evolution of HDPE under different modes of straining and compare the predicted results with experimental data.

Constitutive relations

Crystalline phase. Mechanisms involved in the plasticity of crystalline lamellae of semicrystalline polymers are summarized in the reviews by Bowden and Young[4] and by Haudin[5]. These experimentally observed mechanisms are: crystallographic slip, twinning and stress-induced martensitic transformations. The crystal lattice of HDPE is orthorhombic with lattice parameters $a=7.4$ Å, $b=4.93$ Å and $c=2.54$ Å, where **c** is the crystallographic axis coinciding with the chain direction. Experiments on HDPE have established that crystallographic deformation occurs in the (100)[001], (010)[001], {110}[001], (100)[010], (010)[100], and $\{110\}\langle 1\bar{1}0\rangle$ slip systems, and in the (110) and (310) twinning systems. The stress-induced martensitic transformation from the orthorhombic to the monoclinic lattice in HDPE was also detected by X-ray studies. All of these mechanisms, however, leave the molecular chains inextensible. In this paper the mechanical behaviour and texture evolution for initially isotropic HDPE subject to uniaxial tension and compression, simple shear and plane strain compression are studied. For all of these modes of deformation, there is no experimental evidence for the occurrence of twinning or martensitic transformation in anything more than trace amounts[8,10,11], and then occurring only in the very late stages of deformation. Therefore, we consider crystallographic slip as the only mechanism that accomplishes plastic straining in the crystalline lamellae. Two slip categories operate in the orthorhombic unit cell of HDPE crystals: *chain slip*, with its slip direction parallel to the chain direction, such as (100)[001], (010)[001] and {110}[001] slip systems; and *transverse slip*, with its slip direction perpendicular to the chain direction, such as (100)[010], (010)[100] and $\{110\}\langle 1\bar{1}0\rangle$ slip systems. These slip systems comprise only four linearly independent systems. The addition of twinning and martensitic transformation does not provide the missing degree of freedom due to chain inextensibility, but merely aids transverse slip in achieving transverse shape changes.

The resistances to plastic flow of these slip systems can be measured experimentally using highly textured quasi-single-crystalline HDPE obtained by subjecting initially spherulitic material to large plane strain compression in a channel-die[15]. Recently, Bartczak *et al.*[6] have found that the easiest slip system in such quasi-single-crystalline HDPE is the chain slip (100)[001] and that the other slip systems listed above have higher plastic resistances. Based on their experiments, possible slip systems in the crystalline phase of HDPE are summarized in *Table 1*, with their measured or estimated initial shear resistances normalized to τ_0, the resistance (at room temperature) of the easiest chain slip system, (100)[001].

Table 1 Slip systems of HDPE and their corresponding normalized initial resistances used in the current study

		Normalized resistance g^α/τ_0	
	Slip system	Experimental evidence[a]	Current study
Chain slip	(100) [001]	≡1	≡1
	(010) [001]	>2	2.5
	{110} [001]	>2	2.5
Transverse slip	(100) [010]	1.66	1.66
	(010) [100]	>2	2.5
	$\{110\}\langle 1\bar{1}0\rangle$	2.2	2.2

[a] Measured by Bartczak *et al.*[6]

To derive a constitutive law for the crystalline lamella, we first introduce a viscoplastic power law[18–20] relating the shear rate $\dot{\gamma}^\alpha$ of a given slip system α, to the corresponding resolved shear stress, τ^α, on the same slip system as:

$$\dot{\gamma}^\alpha = \dot{\gamma}_0 \frac{\tau^\alpha}{g^\alpha}\left|\frac{\tau^\alpha}{g^\alpha}\right|^{n^c-1} \tag{1}$$

where $\dot{\gamma}_0$ is a reference strain rate (of the order of $10^{-3}\,s^{-1}$), n^c is the non-linear rate exponent (the inverse rate sensitivity coefficient) and g^α is the shear resistance of slip system α. In the present study we neglect strain hardening and normal pressure effects on the shear resistance, so g^α remains constant during the deformation. The neglect of intrinsic strain hardening in the crystalline lamellae is justified because they are very thin and cannot retain dislocations in them. The plastic shear rate on a slip system is known to be temperature dependent. We consider this temperature dependence to reside in the reference strain rate $\dot{\gamma}_0$, but will not discuss its form further.

Because of chain inextensibility and the associated flow rule embedded in equation (1), the shear rate of each slip system is independent of the normal stress component in the chain direction[21]. To cope with these problems we have introduced some special procedures. Let us denote by $\mathbf{S}^{c*}$, a special modification of the deviatoric Cauchy stress tensor in the crystalline lamella, $\mathbf{S}^c$, with zero normal component in the chain direction (i.e. $S^{c*}_{ij}c_ic_j=0$)[14]. The resolved shear stress in slip system α can then be expressed as $\tau^\alpha = S^{c*}_{ij}R^\alpha_{ij}$, where $\mathbf{R}^\alpha$ is the symmetric, traceless Schmid tensor of stress resolution associated with the slip system α. The components of the symmetric part of the Schmid tensor, R^α_{ij}, can be defined as $R^\alpha_{ij}=\frac{1}{2}(s^\alpha_i n^\alpha_j + n^\alpha_i s^\alpha_j)$, where s^α_i and n^α_i are the components of unit vectors in the slip direction and the slip plane normal, respectively, of the given slip system α.

The plastic strain-rate tensor, $\mathbf{D}^c$, resulting from the contributions of all K active slip systems in the crystalline

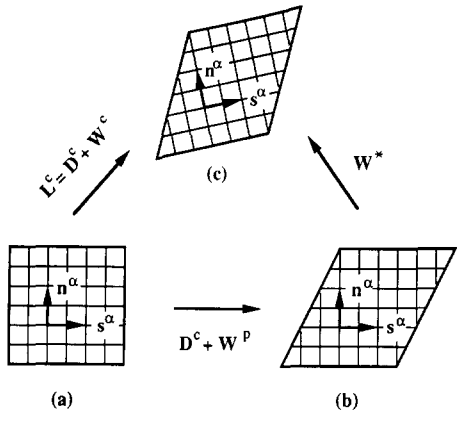

Figure 2 Kinematics of the various components of crystallographic slip and spin: (a) initial undeformed lattice; (b) plastically sheared lattice; (c) plastically sheared and rotated lattice

lamella is given by:

$$D^c_{ij} = \left(\dot{\gamma}_0 \sum_{\alpha=1}^{K} \frac{1}{g^\alpha} \left| \frac{\tau^\alpha}{g^\alpha} \right|^{n^c - 1} R^\alpha_{ij} R^\alpha_{kl} \right) S^{c*}_{kl} \tag{2}$$

Relation (2) represents a three-dimensional constitutive law for the plastic behaviour of the crystalline lamellae through active slip systems and accounts for chain inextensibility, i.e. $D^c_{ij} c_i c_j = 0$, by virtue of the special geometrical restrictions $R^\alpha_{ij} c_i c_j = 0$ present on all available slip systems α, as discussed above.

The principal cause of crystallographic texture development is lattice rotation resulting from the change of external shape in relation to the material lattice. We call the rate of lattice rotation, $\mathbf{W}^*$, the lattice spin tensor. The concepts are illustrated schematically in *Figure 2*. *Figure 2a* illustrates a reference material element in a crystalline domain, along with the unit vectors $\mathbf{n}^\alpha$ and $\mathbf{s}^\alpha$ representing slip plane normal and the slip direction of the slip system α. Without loss of generality, the instantaneous configuration can be taken as the external shape reference. At fixed lattice orientation the rate of crystallographic shearing of a magnitude $\dot{\gamma}^\alpha$ on system α generates a strain rate $\dot{\gamma}^\alpha R^\alpha_{ij}$ and a plastic spin $\dot{\gamma}^\alpha A^\alpha_{ij}$ where $A^\alpha_{ij} = \frac{1}{2}(s^\alpha_i n^\alpha_j - n^\alpha_i s^\alpha_j)$ is the skew part of the Schmid tensor for slip system α, introduced above. The resulting (intermediate) deformed configuration is shown in *Figure 2b*, where it is noted that the total crystallographic strain rate $\mathbf{D}^c$ and plastic spin $\mathbf{W}^p$ are given by the sum over all slip systems K, and represented in purely kinematical form as:

$$D^c_{ij} = \sum_{\alpha=1}^{K} \dot{\gamma}^\alpha R^\alpha_{ij} \quad \text{and} \quad W^p_{ij} = \sum_{\alpha=1}^{K} \dot{\gamma}^\alpha A^\alpha_{ij}$$

We note that homogeneous slipping alone, in general, alters lengths and orientations of material line elements represented by fiducial lines and angles drawn on the element (e.g. 'diagonals' of the material element), but leaves the lattice unchanged. Lastly, the intermediate configuration is subject to a strain free rigid body rotation rate $\mathbf{W}^*$, which carries both material line elements and the lattice vectors to their final orientations. This is shown in *Figure 2c*.

The crystalline velocity gradient $\mathbf{L}^c$ bringing material line elements directly from the initial to the final configuration is: $\mathbf{L}^c = \mathbf{D}^c + \mathbf{W}^c$, as also shown in *Figure 2*. The skew part of this tensor $\mathbf{W}^c$ is the sum of the skew parts due to plastic spin and rigid body spin: $\mathbf{W}^c = \mathbf{W}^p + \mathbf{W}^*$. Thus, the lattice spin controlling the rate of change of crystallographic axes, relative to the initial reference fiducial body axes, can be expressed in terms of total crystallographic spin and the slip rates by:

$$W^*_{ij} = W^c_{ij} - W^p_{ij} = W^c_{ij} - \sum_{\alpha=1}^{K} \dot{\gamma}^\alpha A^\alpha_{ij} \tag{3}$$

The rate of change of crystallographic axes, for instance the chain axis $\mathbf{c}$, can be expressed in component form as:

$$\dot{c} = W^*_{ij} c_j \tag{4}$$

Amorphous phase. Several theories have been proposed for the plastic shear resistance of amorphous polymers in their glassy state[22,23]. In the theory proposed by Argon[23], plastic flow is considered governed by repeated nucleation of local shear transformations consisting of the rotation of short molecular segments under stress*. At room temperature, the amorphous phase of semicrystalline polymers can be in the glassy state, such as in poly(ethylene terephthalate) (PET) and Nylon 6, or in the rubbery state, such as in HDPE. While the theory of Argon is intended only as an isostructural theory for the glassy state — well below the glass transition temperature (T_g) — we will apply a power-law approximation of it to the rubbery state for HDPE. The simple viscoplastic relation that we propose to relate the plastic shear rate $\dot{\gamma}^a$ and the effective shear stress τ^a in the amorphous phase of HDPE is of the form:

$$\dot{\gamma}^a = \dot{\gamma}_0 \left(\frac{\tau^a}{a\tau_0} \right)^{n^a} \tag{5}$$

where $\dot{\gamma}_0$ is a reference strain rate and n^a is the rate exponent. Here, without loss in generality, we choose the reference strain rate equal to that of the crystalline phase.

For simplicity and convenience, we set the rate exponent in the amorphous phase, n^a, equal to n^c, that of the crystalline phase, so $n^a = n^c \equiv n$. The reference shear strength $\tau_0 \equiv g^{(100)[001]}$ is the initial shear resistance of the easiest slip system in the crystalline phase. Thus, $a\tau_0$ is the reference shear strength of the amorphous domain, with the parameter a characterizing the relative magnitude of the initial deformation resistance in the amorphous phase in comparison to that of the easiest slip system in the crystalline phase.

Once the barrier to the chain motion is overcome, the molecular chains of the amorphous phase tend to align in the direction of the maximum plastic stretch, resulting in directionally specific changes in the resistance to plastic flow. To derive a three-dimensional constitutive relation for the amorphous phase, we neglect elasticity and introduce a back stress tensor, $\mathbf{H}^a$, in the flow rule, as was done in the work of Boyce *et al.*[25]. The back stress accounts for the strain hardening produced by molecular alignment. Let $\mathbf{D}^a$ and $\mathbf{S}^a$ be the strain rate (stretching) and the deviatoric Cauchy stress, respectively, present in the amorphous phase. The driving stress (often called effective stress) within the amorphous phase is then

* New molecular segmental level simulations of plastic deformation in glassy polymers, performed by Mott *et al.*[24] have now established that the actual mechanism of this deformation is very different from what was conceived by Argon[23]. Nevertheless, the functional form of the constitutive relation arising from this early work, as also amended by Boyce *et al.*[25], remains as a very accurate formulation of the viscoplastic response of these materials

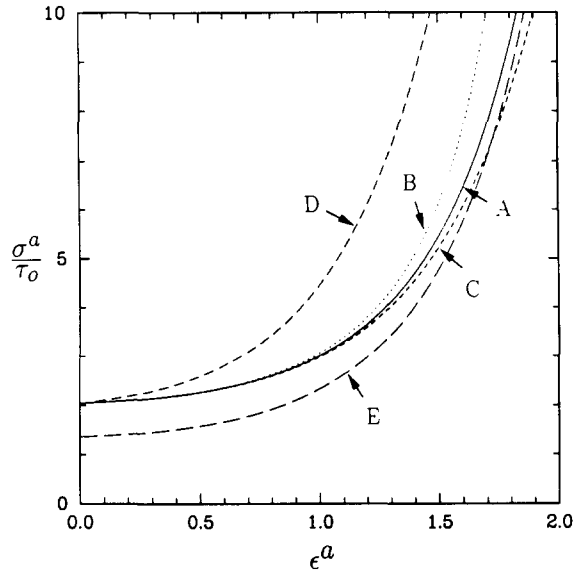

Figure 3 Normalized axial stress, σ^a/τ_0, as a function of the axial logarithmic strain ε^a, for several combinations (a, C^R/τ_0, N) of a pure amorphous polymer of the type modelled here, when deformed homogeneously in uniaxial tension at a fixed reference strain rate $\dot{\gamma}_0$. (A) $a=1.2$, $C^R/\tau_0=0.2$, $N=49$; (B) $a=1.2$, $C^R/\tau_0=0.2$, $N=20$; (C) $a=1.2$, $C^R/\tau_0=0.2$, $N=200$; (D) $a=1.2$, $C^R/\tau_0=0.5$, $N=49$; (E) $a=0.8$, $C^R/\tau_0=0.2$, $N=49$

defined as $\mathbf{S}^a-\mathbf{H}^a$. The resolved shear stress τ^a is defined as a norm of the driving stress by:

$$\tau^a=\sqrt{\tfrac{1}{2}(S^a_{ij}-H^a_{ij})(S^a_{ij}-H^a_{ij})} \tag{6}$$

Generalizing equation (5), the three-dimensional power-law constitutive relation which we propose for the rubbery amorphous polymer is:

$$D^a_{ij}=\dot{\gamma}_0\left(\frac{\tau^a}{a\tau_0}\right)^{n^a-1}\left(\frac{S^a_{ij}-H^a_{ij}}{a\tau_0}\right) \tag{7}$$

Using the eight-chain network model of rubber elasticity recently proposed by Arruda and Boyce[26], the back stress is conveniently expressed as:

$$H^a_{ij}=\frac{C^R}{3}\sqrt{\frac{3N}{I_1}}\,\mathscr{L}^{-1}\left(\sqrt{\frac{I_1}{3N}}\right)(B^a_{ij}-\tfrac{1}{3}I_1\delta_{ij}) \tag{8}$$

where N is the number of rigid links between entanglements and is approximately proportional to the square of the tensile locking stretch, C^R is the rubbery shear modulus, $\mathbf{B}^a$ is the so-called left Cauchy–Green deformation tensor obtained from the deformation gradient tensor $\mathbf{F}^a$ of the amorphous phase ($B^a_{ij}=F^a_{ik}F^a_{jk}$), $I_1=B^a_{ii}$, δ_{ij} is the Kronecker delta and $\mathscr{L}$ is the Langevin function defined by $\mathscr{L}(\beta)=\coth(\beta)-1/\beta=\sqrt{I_1/3N}$, with symbolic inverse function $\mathscr{L}^{-1}(\sqrt{I_1/3N})=\beta$.

For homogeneous uniaxial tensile extension at constant axial strain rate chosen so that $\dot{\varepsilon}^a=\dot{\gamma}_0$, the uniform axial component of the Cauchy stress, σ^a, *versus* logarithmic strain curve is shown in *Figure 3* for $n=9$, for several different combinations of N, C^R/τ_0 and a. The locking of the amorphous polymer due to molecular alignment is shown by a dramatic increase in required stress. The relative strength parameter a scales the initial flow stress, which is also proportional to the nth root of strain rate; a change in the number of rigid links N is primarily accompanied by a change in the final locking stretch; and a change of normalized rubbery shear modulus C^R/τ_0 is accompanied by a change in hardening slope of the stress–strain curve. The simple eight-chain model accurately captures the sensitivity of large deformation rubbery response to states of deformation other than uniaxial tension[26].

Composite inclusion

In the present work, the composite inclusion is treated using a generalized three-dimensional lamination theory, such that the deformation and stress within each phase are uniform (but not necessarily identical) and satisfy the constraints of interface compatibility and equilibrium. Let $\mathbf{D}^I$ and $\mathbf{W}^I$ be the inclusion-averaged strain rate and spin, respectively, that can be expressed as:

$$D^I_{ij}=f^aD^a_{ij}+(1-f^a)D^c_{ij} \tag{9a}$$

and

$$W^I_{ij}=f^aW^a_{ij}+(1-f^a)W^c_{ij} \tag{9b}$$

where superscripts a and c denote the uniform quantities within the amorphous and crystalline phases, respectively. Similarly, the inclusion-averaged deviatoric stress, $\mathbf{S}^I$, can be written as:

$$S^I_{ij}=f^aS^a_{ij}+(1-f^a)S^c_{ij} \tag{9c}$$

We assume that there is no relative slippage at the crystalline/amorphous interface of each inclusion, imposing continuous velocity across each such crystalline/amorphous interface. Let $\mathbf{e}^I_i$ denote local orthonormal Cartesian basis vectors fixed to inclusion I, with $\mathbf{e}^I_3=\mathbf{n}^I$. Relative to this basis, the compatibility conditions, in conjunction with incompressibility in both phases, require the following continuity conditions on strain rate and spin components:

$$D^I_{\alpha\beta}=D^c_{\alpha\beta}=D^a_{\alpha\beta} \tag{10a}$$

$$D^I_{33}=D^c_{33}=D^a_{33} \tag{10b}$$

$$W^I_{12}=W^c_{12}=W^a_{12} \tag{10c}$$

where the Greek subscripts α and β range from 1 to 2.

The requirement of shear traction equilibrium across the interface can be expressed in terms of stress deviator components relative to the local Cartesian basis vectors $\mathbf{e}^I_i$ by:

$$S^I_{\alpha 3}=S^c_{\alpha 3}=S^a_{\alpha 3} \tag{11a}$$

Since we assume incompressibility and neglect pressure sensitivity of deformation, the normal ($\mathbf{n}^I$ or $\mathbf{e}^I_3$) component of interface traction can be equilibrated by assuming that any jump of the normal component of deviatoric stress is balanced by a corresponding jump in the pressure as:

$$S^a_{33}-p^a=S^c_{33}-p^c \tag{11b}$$

where p^a and p^c are the pressure in the amorphous layer and crystalline lamella, respectively.

Interaction law and solution procedure

A local/global interaction relation must be imposed to relate the average mechanical behaviour of each composite inclusion to the macroscopic mechanical behaviour of the medium within which it resides. The collective plastic deformation of aggregates, such as grains in a polycrystalline assembly, has been the subject of many studies in crystal plasticity and mechanics of heterogeneous plastic media. Since exact solutions satisfying all local conditions of equilibrium

and compatibility are intractable, a number of approximate approaches have been developed throughout the years. The most prominent of these are the Sachs model[27], the Taylor model[28] and the self-consistent model[29]. In the Sachs model, local and global equilibrium are satisfied trivially by considering the stress as uniform in all component parts, global compatibility is enforced as a global volume average, while the local compatibility of inclusion deformation with that of its surroundings is not addressed. In the complementary Taylor model, compatibility of deformation is satisfied everywhere by considering the local deformation to be related to the global one in an affine sense, global equilibrium is satisfied only as a global volume average, and local equilibrium of the inclusion with its surroundings is unaddressed. The self-consistent model was first developed to determine the properties of heterogeneous elastic media, and was generalized later in an approximate sense to viscoplastic behaviour. In the self-consistent models, the field solution for a generic ellipsoidal inclusion embedded in a homogeneous 'matrix' medium having as yet undetermined properties and subject to uniform remote fields is first obtained. When the matrix medium is linear elastic (or linear viscous), Eshelby[30] showed that the resulting fields within any ellipsoidal inclusion are homogeneous. Finally the volume averages of all such ellipsoidal inclusion fields are equated to the respective distant mean fields self-consistently to implicitly establish the properties of the effective medium.

In the plasticity of polycrystalline cubic metals, the Taylor model has proved to be the most successful[20] in predicting the plastic resistance of the polycrystal from the plastic resistance of the individual grains. In comparison the Sachs model, while being far easier to implement, has significantly under-predicted the ratio of polycrystal to single crystal deformation resistance because of its lack of intercrystalline deformation constraints. The self-consistent model, which is the most elegant and appealing, is difficult to implement in general in a viscoplastic material. Moreover, it lends itself best to relatively equi-axed morphology and not to the elongated sandwich plate morphology of the crystalline lamellae and amorphous regions making up a semicrystalline polymer. In the past, two of us[21] have successfully applied a modified Taylor formulation to an idealized model of HDPE consisting of crystalline aggregates alone. Textures were successfully predicted for several different modes of straining, but the texture evolved much too rapidly with deformation, and predicted aggregate plastic stress–strain response did not compare well with corresponding experimental measurements. We had also previously attempted to obtain more realistic stress–strain curves by incorporating an amorphous material component into a generalized Taylor model, using constitutive properties similar to those given in the section 'Constitutive relations'[31,32]. However, it became apparent that in order to achieve realistic stress–strain response, unrealistic properties needed to be assigned to the amorphous component, which then significantly degraded the texture-predicting ability of the model[31,32]. The severe constraint of crystalline phase inextensibility particularly manifested itself in those composite inclusions for which the inclusion normal $\mathbf{n}^I$ became nearly parallel with the chain axis $\mathbf{c}$ during the course of deformation[14]. As a result, it was concluded that since local deformation within the composite inclusion is already constrained, due to both crystalline phase inextensibility and to the compatibility enforced between the crystalline and amorphous layers, it is less important to further constrain the deformation of the composite inclusion by enforcing additional local compatibility restrictions between the inclusion and the matrix, than it is to provide local equilibrium of the composite inclusion with its surroundings. Consequently, we have developed a modified Sachs-like interaction rule for each composite inclusion which satisfies equilibrium, both strongly within the inclusion and somewhat less strongly between the inclusion and its surroundings, but satisfies compatibility only as a global volume average of the locally compatible deformations and spins of the individual composite inclusions. In our new proposed composite model, a Sachs-like interaction law is employed. As demonstrated in reference 14, the Sachs interaction law for composite inclusions is applicable to the study of large plastic deformation and texture evolution in semicrystalline polymers under different loading conditions.

Consider an aggregate of composite inclusions subject to macroscopically applied boundary conditions consistent with homogeneous response. Let us denote by $\bar{\mathbf{S}}$, $\bar{\mathbf{D}}$ and $\bar{\mathbf{W}}$ the macroscopic deviatoric Cauchy (true) stress, the macroscopic strain rate, and the macroscopic spin, respectively. Relative to the fixed macroscopic orthonormal basis vectors $\bar{\mathbf{e}}_i$, specific components of $\bar{S}_{ij}$, $\bar{D}_{ij}$ and $\bar{W}_{ij}$ must be prescribed in accordance with a well-posed boundary value problem. For example, in the case of constant strain rate uniaxial tension or compression along the $\bar{\mathbf{e}}_3$ direction, the prescribed components of $\bar{\mathbf{S}}$, $\bar{\mathbf{D}}$ and $\bar{\mathbf{W}}$, relative to the basis vectors $\bar{\mathbf{e}}_i$, are:

$$\bar{D}_{33} \neq 0 \tag{12a}$$

$$\bar{S}_{22} - \bar{S}_{11} = \bar{S}_{12} = \bar{S}_{13} = \bar{S}_{23} = 0 \tag{12b}$$

and

$$\bar{\mathbf{W}} = 0 \tag{12c}$$

The other (five) (work-conjugate) components of $\bar{\mathbf{S}}$ and $\bar{\mathbf{D}}$ which are not prescribed must be obtained from conditions of global compatibility and equilibrium.

In applying the Sachs inclusion model, the inclusion-averaged deviatoric stress in each inclusion, $\mathbf{S}^I$, is approximated as constant, and equal to the macroscopic deviatoric stress, $\bar{\mathbf{S}}$, imposed on the aggregate such that:

$$\mathbf{S}^I = \bar{\mathbf{S}} \tag{13a}$$

To complete the interaction law of a Sachs inclusion model for large deformation, we simply equate the inclusion-averaged spin, $\mathbf{W}^I$, with the macroscopic one, $\bar{\mathbf{W}}$:

$$\mathbf{W}^I = \bar{\mathbf{W}} \tag{13b}$$

The self-consistent conditions for global equilibrium and compatibility within the aggregate[33] are that suitable volume averages of local fields equal the corresponding macroscopic quantities. The Sachs inclusion model of equations (13a) and (b) satisfies the following requirements trivially:

$$\langle \mathbf{S}^I \rangle = \bar{\mathbf{S}} \tag{14a}$$

$$\langle \mathbf{W}^I \rangle = \bar{\mathbf{W}} \tag{14b}$$

where $\langle \cdot \rangle$ designates the volume average over the

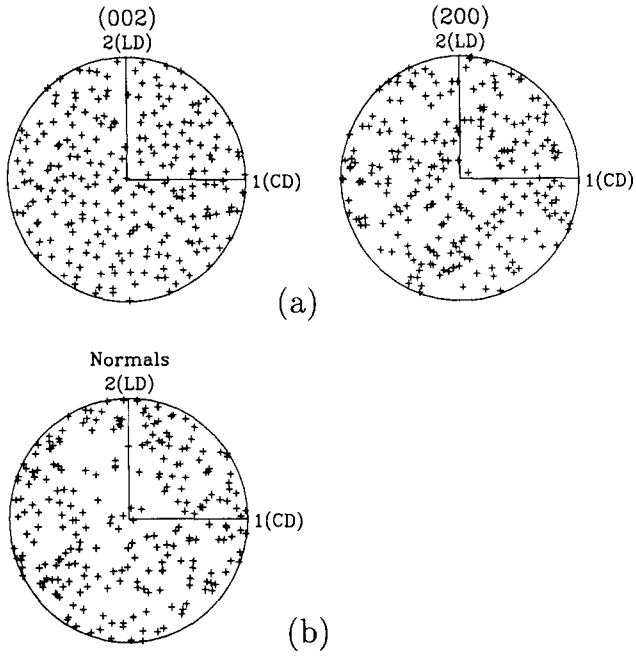

Figure 4 Pole figures from 244 randomly oriented composite inclusions represent the initially isotropic texture for undeformed HDPE: (a) crystallographic texture; (b) distribution of lamellar normals

aggregate. The remaining self-consistent conditions provide global compatibility, i.e. the volume average of the inclusion strain rate must equal the macroscopic strain rate:

$$\langle \mathbf{D}^{\mathrm{I}} \rangle = \bar{\mathbf{D}} \tag{14c}$$

In practice, the volume integrals indicated in equations (14a)–(c) are replaced with integrals over the collection of inclusions representing the material, and the volume-averaged fields within each composite inclusion are weighted equally when computing the macroscopic average fields.

When using the Sachs inclusion interaction law, equations (14a) and (c) can be used to obtain the five components of $\bar{\mathbf{S}}$ and $\bar{\mathbf{D}}$ not specified in the definition of the macroscopic boundary value problem. Full details of the solution procedure are beyond the scope of this paper but can be found in reference 14. To simulate the large plastic deformation of semicrystalline polymers, the evolution of texture in these materials has to be taken into account, and is, of course, of primary interest here. Procedures for updating the crystallographic, morphological, and macromolecular textures during the numerical simulation can also be found in reference 14 and will be omitted here.

Parameter selection

Consider an aggregate consisting of M composite inclusions as described above. This aggregate may represent an isotropic or even oriented semicrystalline polymer depending on the initial orientation distribution assigned to this set of inclusions. We consider an initially isotropic HDPE and neglect interactions between spherulites so that the initial spherulitic morphology is not accounted for explicitly. However, it is possible to generate an isotropic texture corresponding to a 'quasi-spherulitic' structure. In the modelling of initially isotropic HDPE, an aggregate consisting of 244 composite inclusions is employed. The initial distributions of crystallographic orientations given by the (002) pole figures (or chain axis, **c**) and (200) pole figures (or **a**-axis) are shown in equal area stereographic projection in *Figure 4a* for these 244 inclusions. Since the distributions of (002) and (200) pole figures are essentially uniform [also true for the (020) pole figure due to the orthogonality of crystal axes], the initial crystallographic texture of the aggregate can be considered as isotropic. It has been reported[34–36] that for spherulitic polyethylene, the chain axis **c** and the lamellar normal $\mathbf{n}^{\mathrm{l}}$ are not parallel. The initial angle between these two axes varies between 17° and 40°. An isotropic initial distribution of lamellar normals can then be obtained by assuming an initial angle of 30° between **c** and the corresponding $\mathbf{n}^{\mathrm{l}}$, along with a random projection of $\mathbf{n}^{\mathrm{l}}$ in the local crystal plane spanned by **a** and **b**. The initial distribution of lamellar normals for these 244 inclusions is shown in *Figure 4b*.

For the (common) strain-rate sensitivity exponent, we use the value $n=9$ in each phase, based on the measurements of macroscopic rate sensitivity in HDPE reported by G'Sell and Dahoun[37]. A typical level of crystallinity of HDPE is ~70%; therefore, in the following applications, $f^{\mathrm{a}}=0.3$ is used in the modelling of HDPE. We first apply the proposed composite model to the aggregate consisting of 244 composite inclusions to predict the uniaxial reference strength, $\bar{\sigma}_0$, of initially isotropic HDPE in the following power-law creep equation:

$$\bar{D}^{\mathrm{eq}} = \dot{\gamma}_0 \left(\frac{\bar{\sigma}^{\mathrm{eq}}}{\bar{\sigma}_0} \right)^n \tag{15}$$

where $\bar{D}^{\mathrm{eq}} = \sqrt{\frac{2}{3}\bar{D}_{ij}\bar{D}_{ij}}$ and $\bar{\sigma}^{\mathrm{eq}} = \sqrt{\frac{3}{2}\bar{S}_{ij}\bar{S}_{ij}}$ are the macroscopic equivalent uniaxial tensile strain rate and stress, respectively. This uniaxial reference strength, $\bar{\sigma}_0$, normalized by the resistance of the easiest slip system, τ_0, is plotted in *Figure 5* as a function of the strength coefficient a of the amorphous domain. It is emphasized that the macroscopic reference strengths shown in *Figure 5* are isostructural, reflecting no alterations due to deformation-driven texturing or molecular orientation. Since $\bar{\sigma}_0$ depends parametrically on the strength coefficient a of the amorphous domain, and since the amorphous interlamellar material is itself inaccessible to

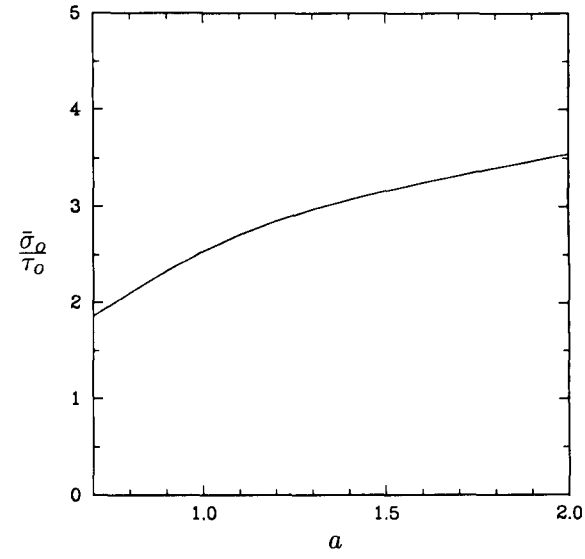

Figure 5 Normalized uniaxial reference strength, $\bar{\sigma}_0/\tau_0$, as a function of the amorphous domain strength coefficient a

mechanical testing, we use experimental measurements and the model to infer an appropriate value for a.

In the literature, experimentally based estimates of the resistance of the easiest slip system, $g^{(100)[001]}$, at room temperature range between $\tau_0 = 7.2$ MPa (ref. 6) and $\tau_0 = 9.0$ MPa (ref. 17). A partial explanation for this difference is the fact that interpretation of experimental measurements of τ_0 is complicated by the presence of amorphous material, rendering even highly textured material a composite. At room temperature, the measured tensile yield strength[7,8] of initially isotropic, spherulitic HDPE is ~27 MPa. In order to obtain a reasonable correlation of yield strength in the aggregate with chain slip resistance, $\bar{\sigma}_0/\tau_0$ should have a value between 3.0 and 3.75. Thus, based on *Figure 5*, in the following applications, the amorphous domain strength coefficient a is chosen to be 1.2 (see ref. 14). We also choose the number of rigid links as $N = 12$ and rubbery modulus $C^R = 0.1\tau_0$ for the amorphous phase so that the predicted macroscopic stress–strain curve of the HDPE in uniaxial compression corresponds to experiments[7], with reasonable locking stretch and strain hardening slope. Before these final values were chosen, the effects of the amorphous phase material constants (a, N, C^R) on the macroscopic stress–strain response were studied parametrically, based on the uniaxial compression test, to obtain the best fit. An account of this can be found elsewhere[14].

PREDICTED RESULTS AND COMPARISON WITH EXPERIMENTS

Modes of straining

We have applied the proposed composite model to simulate stress–strain response and texture evolution in initially isotropic HDPE for several different modes of straining. Predicted results are compared with both the experimental results of previous investigators and with the results of our own recent extensive experiments. The different modes of straining that were considered are constant strain rate uniaxial tension and compression, simple shear and plane strain compression. According to their deformation patterns, these modes of straining can be divided into two major classes: *convergent* molecular flow, with only one principal stretch greater than unity, such as in uniaxial tension; and *divergent* molecular flow, with two principal stretches greater than unity, such as in uniaxial compression. Intermediate to these classes are cases of *neutral* molecular flow, with one principal stretch remaining unity, such as plane strain compression and simple shear.

The common denominator of these two classes of deformation is that in convergent molecular flow, as well as in neutral flow, a process of fragmentation of stretched lamellae or stretching out of lamellae into microfibrils ultimately occurs in the course of deformation. In the case of tension and plane strain compression (also rolling) this results in a major restructuring of crystalline and amorphous domain morphology into a new long period and the establishment of a new family of lamellae. In simple shear the replacement of stretched out lamellae into microfibrils is not followed by a restructuring to form a new long period. The reasons for this are not clear[10]. These phenomena introduce into the deformation important additional considerations such as interface migration and redistribution of packing defects among chains. Such restructuring is not detected in the latter class of divergent deformation. In the following sections, we first present the predicted results and then compare them with experimental observations for the class of divergent molecular flow, followed by those for the class of convergent molecular flow, up to the point where the above-mentioned morphological restructuring phenomena occur.

Uniaxial compression

The first application is the prediction of the stress–strain response and texture evolution in HDPE deformed under constant strain rate uniaxial compression (with $\bar{D}^{eq}/\dot{\gamma}_0 = 1$). The calculated equivalent macroscopic stress, $\bar{\sigma}^{eq}$, is plotted *versus* equivalent macroscopic strain, $\bar{\varepsilon}^{eq} = \int_0^t \bar{D}^{eq}\,dt$ in *Figure 6*. Also shown in *Figure 6* are the corresponding curves for the other deformations, which will be discussed further below. As can be seen from *Figure 6*, our predicted compressive curve compares well with the experimental data obtained by Bartczak *et al.*[8] (to which it was fitted), including the level of locking stretch and strain hardening slope. Parenthetically, we note that the predicted stress–strain curves in *Figure 6* show a jerky behaviour. The frequent, short stress drops result from the Sachs inclusion model when, during the course of deformation, certain composite inclusions, by assumption subject to inclusion average stress $\mathbf{S}^I = \bar{\mathbf{S}}$, are momentarily caught in 'soft' orientations. Such model inclusions tend to experience local 'runaway' deformation rate until their accumulating local deformation and accompanying rotation and amorphous phase orientation hardening naturally rectify the soft condition. Meanwhile, however, the accelerated macroscopic volume average deformation rate, in conjunction with the rate sensitivity of flow, results in the stress drops. As discussed elsewhere[14], we have successfully rectified this relatively benign aberration by the introduction of a more sophisticated self-consistent-like model which is considerably more difficult to implement; however, overall results of the more elaborate model do not differ much from the

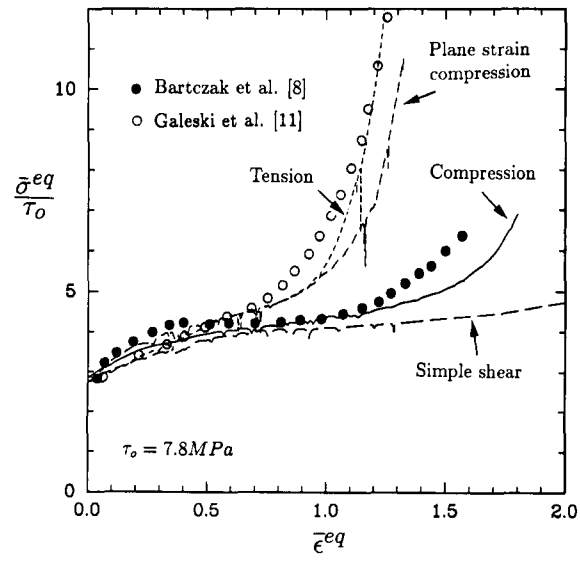

Figure 6 Normalized equivalent macroscopic stress, $\bar{\sigma}^{eq}/\tau_0$, as a function of the equivalent macroscopic strain, $\bar{\varepsilon}^{eq}$, for initially isotropic HDPE subject to different modes of straining. Experimental data points shown were normalized using $\tau_0 = 7.8$ MPa (see refs 8 and 11)

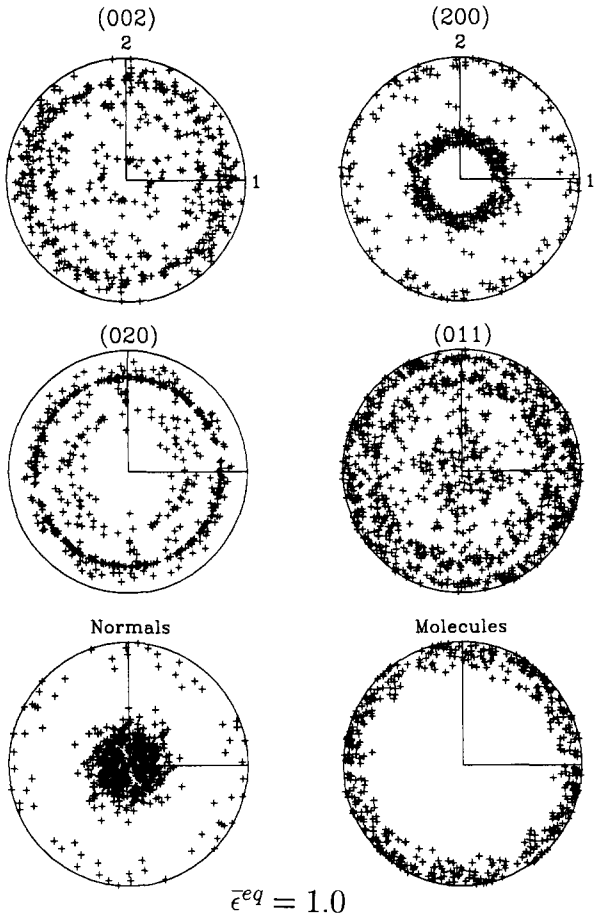

Figure 7 Predicted crystallographic textures, morphological texture (lamellae normals) and the amorphous phase molecular alignment for HDPE subject to uniaxial compression at $\bar{\epsilon}^{eq} = 1.0$. Pole figure labelled 'molecules' shows axes of maximum principal stretch in amorphous domains of each inclusion. (Compressive direction is along the 3-axis)

smoothed results of the Sachs inclusion model considered here.

Figures 7 and *8* give the predicted crystallographic textures for equivalent strains of 1.0 and 1.8, respectively. In each pole figure, the axis perpendicular to the projection plane is the compression direction. An equal area stereographic projection is used for each pole figure. Note that since the initially chosen 244 inclusions give relatively sparse information in the pole figures for strained material, the pole concentration was enriched by reflecting every pole point with respect to the central point in the pole plots, which for this deformation mode should be a centre of symmetry. *Figures 7* and *8* show that with increasing compressive strain, the poles of the (200) planes (the planes with the lowest chain slip resistance) migrate toward the compression direction, and that the poles of the (002) and (020) planes tend to align circumferentially uniformly in the radial direction. However, in both cases, the final goals — i.e. for the (200) poles to reach the compression axis and for the (002) and (020) poles to reach the radial direction — are not attained. The (011) planes also spread towards the radial direction and evacuate the centre of the pole figure (compression direction) as strain increases. The predicted morphological texture (distribution of the lamellar normals) and macromolecular texture (distribution of orientations of maximum principal stretch within the amorphous layers) are also plotted in *Figures 7* and *8*. With increasing strain, the normals to the crystalline/amorphous interfaces strongly congregate around the compression axis, and molecular segment alignment in the amorphous domains becomes strongly focused toward the radial direction.

At large macroscopic strain, predicted crystallographic textures clearly show two general groups of crystals: a larger group with **a**-axes oriented ~ 20–$30°$ away from the compression direction and both **b**- and **c**-axes oriented toward the radial direction; and a smaller group having their **b**-axes oriented ~ 20–$30°$ away from the compression direction and both **a**- and **c**-axes oriented toward the radial direction. This texture agrees with the experimental observations of Krause and Hosford[38].

Detailed experimental studies of uniaxial compression on HDPE were also made by Bartczak *et al.*[8]. *Figures 9a–c* show the wide-angle X-ray scattering (WAXS) intensity profiles of the (200), (020) and (011) planes as a function of altitude angle measured away from the compression direction for a number of equivalent macroscopic strain levels. The experimental results of *Figure 9a* confirm the model predictions that the scattered intensity of the (200) planes shows a peak at an altitude angle $\sim 25°$ away from the compression direction, while those of *Figure 9c* show that the intensity of the (011) planes generally increases as the altitude angle increases away from the compression direction. Between strains of $1.0 \leqslant \bar{\epsilon}^{eq} \leqslant 1.8$, the model (011) pole figures in *Figures 7* and *8* show a clearing of the region of altitude angles $< 35°$, the development of a monotonically

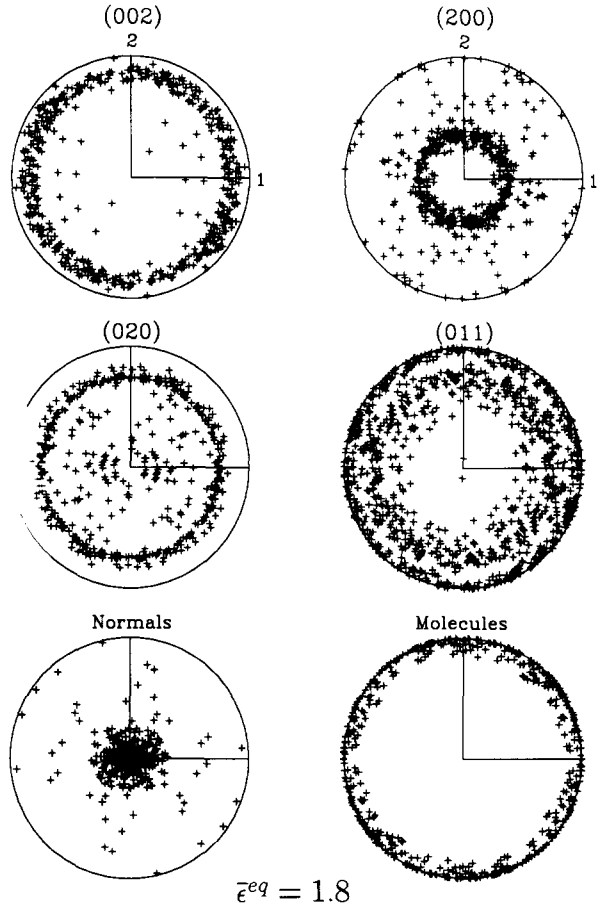

Figure 8 Predicted crystallographic textures, morphological texture and the amorphous phase molecular alignment for HDPE subject to uniaxial compression at $\bar{\epsilon}^{eq} = 1.8$. (Compressive direction is along the 3-axis)

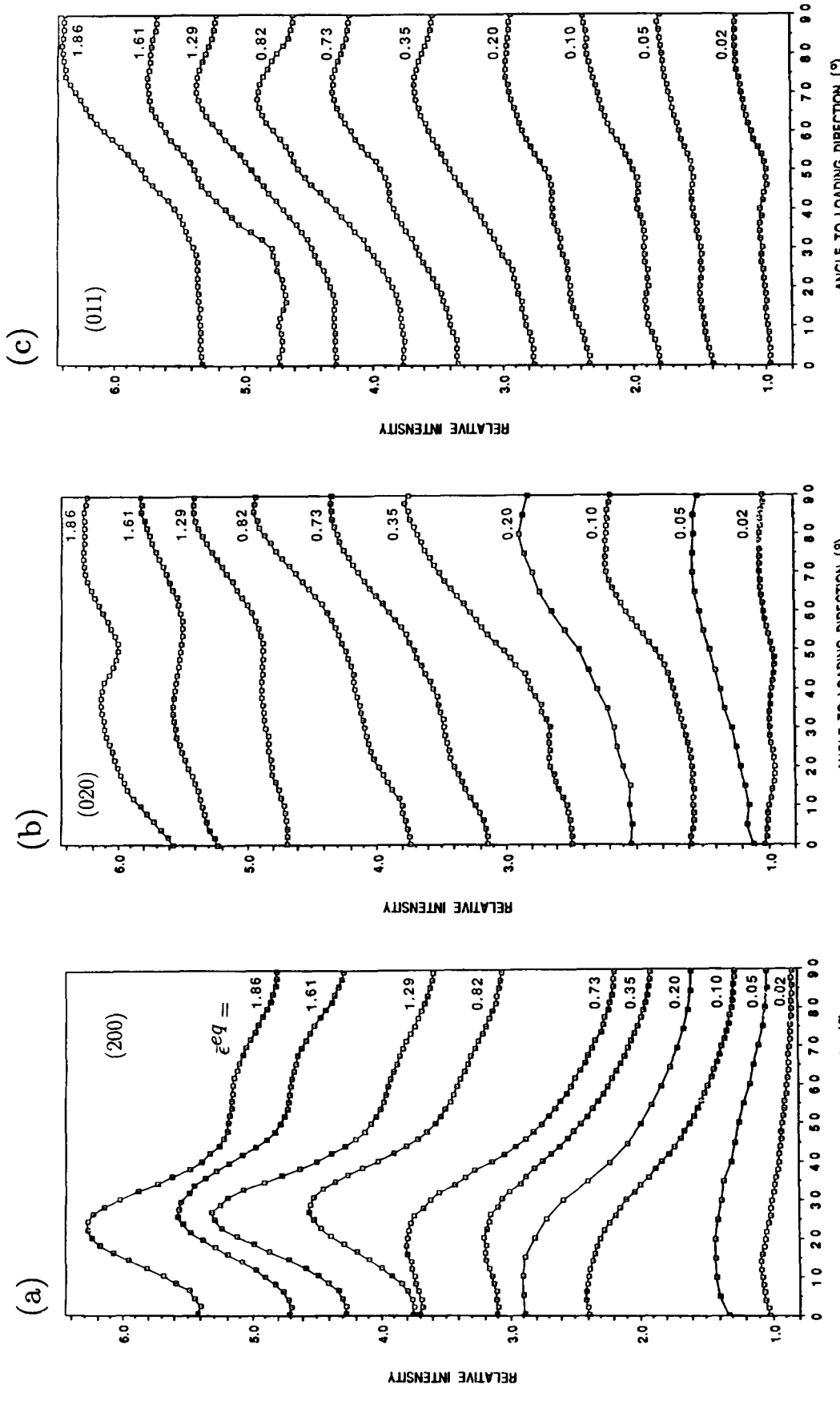

Figure 9 Plots of the WAXS intensities of the diffraction by particular crystallographic planes on the altitude angle between the plane normal and the loading direction at different macroscopic strains of HDPE subject to uniaxial compression: (a) (200) plane; (b) (020) plane; (c) (011) plane. The curves were shifted along the intensity axis for clarity[8]

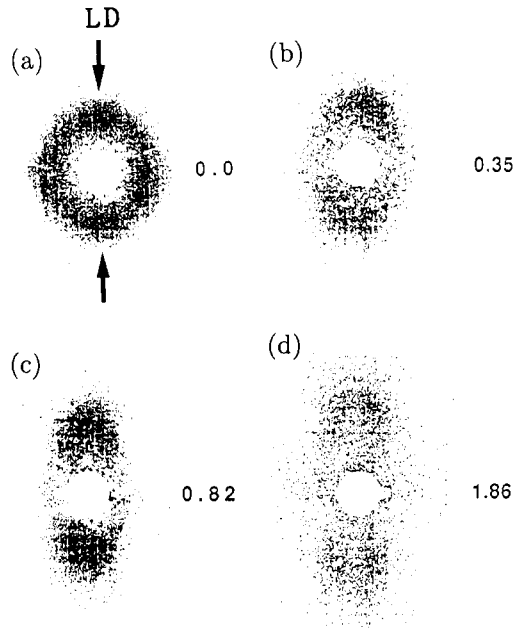

Figure 10 Plots of SAXS patterns viewed from the radial direction for $\bar{\varepsilon}^{eq}$ values of (a) 0, (b) 0.35, (c) 0.82 and (d) 1.86 (see ref. 8). Vertical arrows in (a) indicate uniaxial compression loading direction

increasing intensity within 35–70° altitude, where a weak peak appears, and a filling-in of the region with altitude >70°. These features are in remarkable agreement with experimental trends shown in *Figure 9c*. At the highest strains, the scattered intensity of the (020) planes in *Figure 9b* shows a broad bimodal distribution. These results are consistent with the numerical predictions that there are two groups of crystal orientation[38], a conclusion which is especially evident in the (020) pole figure of *Figure 7* at $\bar{\varepsilon}^{eq} = 1.0$. It is difficult to collect direct WAXS measurements of the (002) planes because of the very low signal-to-noise ratio for the (002) diffraction peak[8]. However, the orientation of the (002) poles (or chain directions) may be deduced from either (200) and (020) pole figures or from the pole figures for (011) and (020) planes. Experimental results support the prediction that the (002) pole of sheared crystalline lamellae progressively aligns in the directions of divergent radial flow.

The monotonic migration of lamellar normals toward the compression axis predicted in *Figures 7* and *8* is best shown experimentally in the small-angle X-ray scattering (SAXS) patterns of Bartczak *et al.*[8]. *Figure 10* shows the SAXS patterns of the deformed material viewed from a radial direction. *Figure 10a* shows the initial isotropic SAXS (uniform ring) pattern of the undeformed sample. The uniform radial distribution of intensity reflects the distribution of long period spacing, or lamellar thickness. At an equivalent strain of 0.35 (*Figure 10b*), a distinct clustering of the SAXS intensity in the region closer to the compression direction is discernible, as well as a perceptible outward motion of the maximum of the intensity peak. This clustering of lamellae sharpens further as an equivalent strain of 0.82 (*Figure 10c*) is reached, where a definite congregation of the lamellar normals has taken shape in the compression direction region, with a further outward motion of the intensity peak, indicating continued compression-induced thinning of the planar lamellae. Finally, in *Figure 10d*, at an equivalent strain of 1.86, the location of the intensity maximum has moved out much further, but the overall scattering has also decreased, indicating further thinning of the lamellae, with lamellar normals now being aligned predominantly parallel to the compression direction, but showing a larger variation in thickness and becoming less regular.

Idealized SAXS patterns of deformed HDPE can be constructed numerically at each stage of deformation based on the calculated orientation of lamellar normals, $\mathbf{n}^l$, and corresponding lamellar thicknesses of the 244 composite inclusions. In the numerical construction of the SAXS pattern, each composite inclusion is represented by two centrally symmetric diffraction points in a polar coordinate plane with the radial distance of the points from the origin proportional to the reciprocal of the lamellar thickness. The angle of the point in the synthesized SAXS pattern is in the same direction as the projection of the lamellar normal on the plane perpendicular to the direction of viewing (or incident beam). Because all computational inclusions were initially of identical thickness, the numerical SAXS pattern at zero strain would show all points at equal radius from the origin, in contrast with the distribution of long periods experimentally noted in *Figure 10a*. This lack of initial thickness distribution in the computational results must be kept in mind when comparing the predicted and experimental SAXS patterns. *Figure 11* shows the numerically constructed SAXS patterns viewed from a radial direction of the uniaxial compression test for macroscopic equivalent strains of 0.5, 1.0 and 1.5, respectively. Both the numerically constructed and the experimental SAXS patterns indicate that, as strain increases, the SAXS images change progressively from a uniform ring pattern to an elliptic pattern with the longer axis aligned with the compression direction, to an eventual two-point pattern. This change in SAXS patterns implies that the lamellar normals migrate toward the compression direction (as is also evident in *Figures 7* and *8*) and that the lamellae that are oriented perpendicular to the compression direction show both a decrease in thickness and an increasing spread in this thickness. The number of lamellae oriented parallel to the compression direction (normals perpendicular to

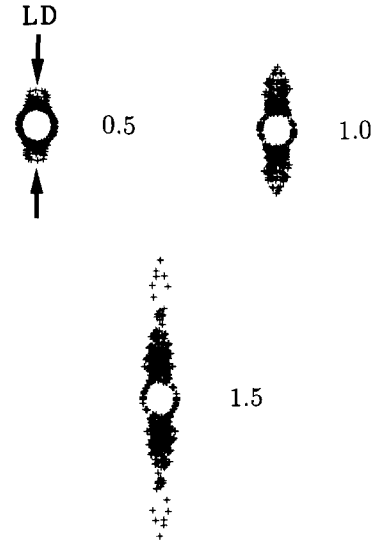

Figure 11 Plots of numerically constructed SAXS patterns for uniaxial compression, viewed from a radial direction, for $\bar{\varepsilon}^{eq}$ values of 0.5, 1.0 and 1.5

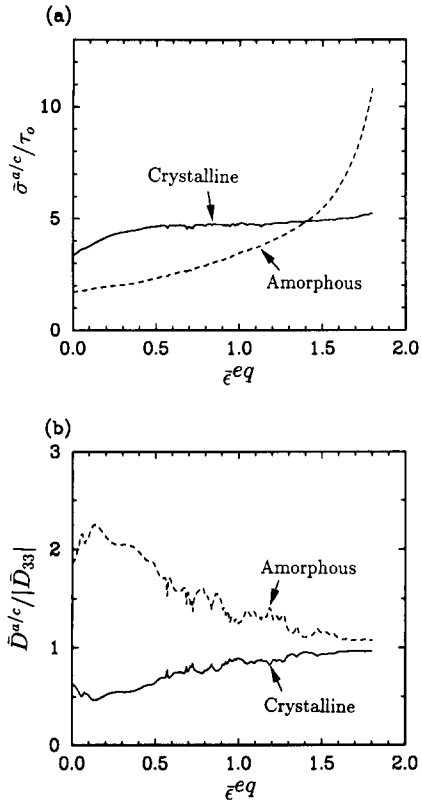

Figure 12 (a) Equivalent phase-volume-averaged stress ($\bar{\sigma}^a$, amorphous; $\bar{\sigma}^c$, crystalline), normalized by τ_0, as functions of $\bar{\varepsilon}^{eq}$; and (b) the equivalent phase-volume-averaged strain rate ($\bar{D}^a$, amorphous; $\bar{D}^c$, crystalline), normalized by the applied macroscopic strain rate, as functions of $\bar{\varepsilon}^{eq}$ in unaxial compression

compression direction) monotonically decreases, while their thickness progressively increases. These features are all in very good agreement with the experimental observations of Bartczak *et al.*[8], shown in *Figure 10*.

In order to gain more understanding regarding the roles of the crystalline and amorphous phases in the texture evolution, the equivalent phase-volume-averaged stretching and stress are calculated for each phase. The equivalent phase-volume-averaged strain rate and stress in the crystalline domains are defined as:

$$\bar{D}^c = \sqrt{\tfrac{2}{3}\lfloor D^c_{ij}\rfloor\lfloor D^c_{ij}\rfloor} \tag{16a}$$

$$\bar{\sigma}^c = \sqrt{\tfrac{3}{2}\lfloor S^c_{ij}\rfloor\lfloor S^c_{ij}\rfloor} \tag{16b}$$

where $\lfloor\cdot\rfloor$ denotes the volume average over the domain occupied by the designated phase. The equivalent phase-volume-averaged strain rate and stress in the amorphous domains, $\bar{D}^a$ and $\bar{\sigma}^a$, can be analogously defined. The normalized equivalent phase-volume-averaged strain rate and stress obtained in this manner for each domain are plotted in *Figure 12 versus* $\bar{\varepsilon}^{eq}$. At low strain, the amorphous phase carries less stress and deforms considerably more rapidly than the crystalline phase. As deformation progresses, the amorphous phase hardens due to network locking, resulting in near equalization of the equivalent phase-volume-averaged strain rates. Strong amorphous phase hardening is seen in *Figure 12a* at $\bar{\varepsilon}^{eq} \geqslant 1.5$; in *Figure 6*, rapid macroscopic hardening in uniaxial compression begins at a similar point. Similarly, the relative magnitude of crystalline phase deformation rate steadily increases with increasing large strain, comparing well with the considerable sharpening of crystallographic texture, evident in *Figures 7* and *8*. Referring to the crystallographic texture shown in *Figures 7* and *8*, we interpret the behaviour as resulting from a competition of chain slip and shearing of amorphous domains that allows the (200) poles to reach a 'stand-off' orientation away from the compression direction as shown in both experimental observation and numerical simulation.

Simple shear

In the case of constant strain rate simple shear (with shear strain rate $\dot{\bar{\gamma}}/\dot{\gamma}_0 = 1$), the calculated plot of $\bar{\sigma}^{eq}$ *versus* $\bar{\varepsilon}^{eq}$ is included in *Figure 6*. The textural hardening developed in simple shear is quite small, in agreement with experimental observations[9,10]. However, it is important to point out that the predicted equivalent stress–strain curve exhibits more strain hardening than that reported by G'Sell *et al.*[9]. This is in part because G'Sell *et al.*[9] neglected the contribution due to (non-zero) macroscopic normal stresses, and set the equivalent macroscopic stress in simple shear equal to $\sqrt{3}\bar{\tau}$, where $\bar{\tau}$ is the macroscopically measured shear stress. The calculated values of $\sqrt{3}\bar{\tau}$ and $\bar{\sigma}^{eq}$ in simple shear are plotted *versus* $\bar{\varepsilon}^{eq}$ in *Figure 13*. The neglected contribution of macroscopic normal stresses to $\bar{\sigma}^{eq}$ is not negligible when $\bar{\varepsilon}^{eq}$ is large. By comparing the curve of calculated $\sqrt{3}\bar{\tau}$ *versus* $\bar{\varepsilon}^{eq}$ with the experimental results reported in G'Sell *et al.*[9], good qualitative agreement is obtained.

Figures 14 and *15* show the predicted crystallographic texture, the distribution of lamellar normals, and the molecular alignment in the amorphous phase at simple shear deformations corresponding to $\bar{\varepsilon}^{eq} = 1.0$ and 2.0, respectively (simple shear strain $\bar{\gamma} = \sqrt{3}$ and $2\sqrt{3}$, respectively). In each pole figure, the neutral x_3 direction is perpendicular to the projection plane, and the direction of the imposed shear is marked. Upon increasing strain, the (002) poles (or chain axes) cluster and rotate toward the direction of maximum stretch (which asymptotically approaches the shear direction), and the (200) poles tend to concentrate around the in-plane direction perpendicular to the direction of

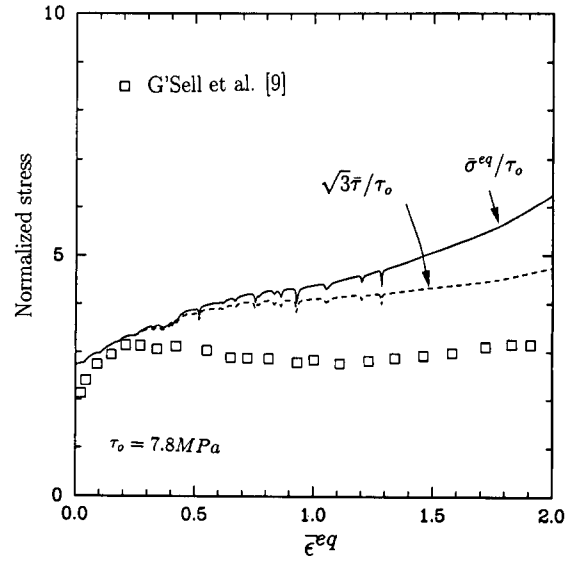

Figure 13 Calculated values of $\sqrt{3}\bar{\tau}/\tau_0$ and $\bar{\sigma}^{eq}/\tau_0$ in simple shear, as functions of $\bar{\varepsilon}^{eq}$. Experimental data points shown were normalized using $\tau_0 = 7.8$ MPa

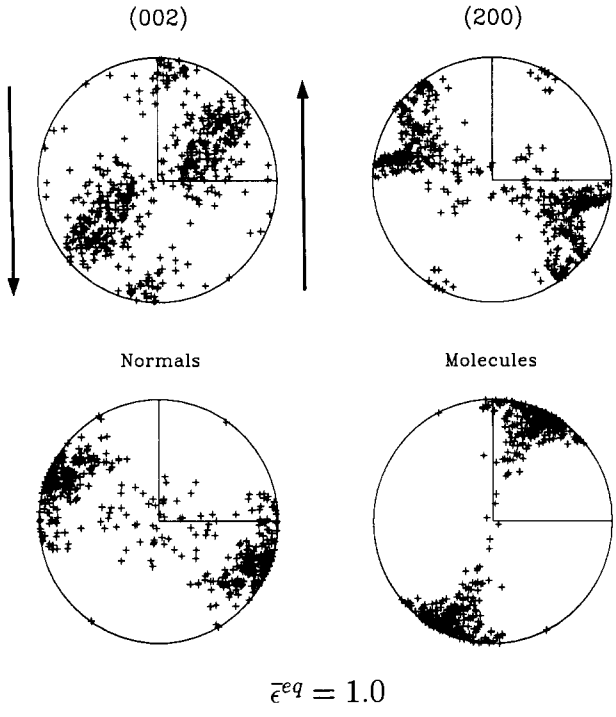

Figure 14 Predicted crystallographic textures, morphological texture (lamellae normals) and the amorphous phase molecular alignment for HDPE subject to simple shear at $\bar{\varepsilon}^{eq} = 1.0$. Arrows indicate sense of applied simple shearing

maximum stretch. The orientation of maximum stretch in the amorphous domains rotates toward the direction of maximum macroscopic stretch in coincidence with the **c**-axes of the crystalline phase. The lamellar normals $\mathbf{n}^l$ rotate toward the opposite and orthogonal in-plane direction, in coincidence with the **a**-axes of the crystalline phase. According to the predicted crystallographic texture, we conclude that the evolution of the texture under simple shear allows most of the deformation, within the crystalline phase, to be accommodated by the lowest resistance (100)[001] chain slip system, producing negligible textural hardening. Such textural interpretations of limited hardening in simple shear were made previously by Parks and Ahzi[21]. The present model also suggests that in simple shear, the amorphous layers do not continue to shear indefinitely.

Figure 16 shows the WAXS patterns of the (002) and (200) plane reflections of samples subjected to simple shear strains of $\bar{\gamma} = 1.8$ ($\bar{\varepsilon}^{eq} = 1.04$) and $\bar{\gamma} = 3.0$ ($\bar{\varepsilon}^{eq} = 1.73$), as obtained by Bartczak *et al.*[10]. Comparison of these intensity patterns of the pole figures with the predicted patterns given in *Figures 14* and *15* shows very good general agreement.

The lamellar morphology can be investigated by the SAXS technique. The results of the SAXS patterns obtained by Bartczak *et al.*[10] with the incident beam parallel to the x_3-axis (i.e. perpendicular to the shear plane) are shown in *Figure 17* for $\bar{\gamma} = 1.8$, 3.0 and 4.3 ($\bar{\varepsilon}^{eq} = 1.04$, 1.73 and 2.48), respectively. The corresponding numerically constructed SAXS patterns for $\bar{\varepsilon}^{eq} = 1.0$, 1.5 and 2.0 are shown in *Figure 18*. It is evident that the predicted SAXS patterns are in good qualitative agreement with the experimental results. As strain increases, the SAXS patterns change smoothly from a uniform ring pattern to a tilted diffused two-point pattern with the long axis of the pattern aligned near the in-plane direction perpendicular to the shearing direction. Both predictions and experiments confirm that the lamellar normals rotate toward the in-plane direction perpendicular to the shear direction, and that the thickness of deformed lamellae decreases.

At very large strains, exceeding 2.0 the sheared lamellae become unravelled and as a result a fibre texture develops resembling that in uniaxial tension. Whether this is an unavoidable kinematic necessity or an artifact of the straining arrangement is unclear[10]. The effects, of course, have not been considered in our model.

Uniaxial tension

For the constant strain rate uniaxial tension test (with $\bar{D}^{eq}/\dot{\gamma}_0 = 1$), the calculated equivalent stress–strain curve is included in *Figure 6*. In an actual tensile test, deformation instabilities (e.g. necking, cavitation) will occur during the deformation[38,39]. Thus, when amorphous material constants are chosen to match uniaxial compression data, where no deformation instability has been reported[8], the predicted macroscopic tensile response in a simulation which neglects cavitation tends to exceed macroscopic experimental measurements of material resistance. Indeed, the calculated stress–strain response in uniaxial tension exhibits somewhat higher strain hardening slope and smaller locking stretch than is experimentally observed[7]. As demonstrated in reference 14, the shape of the predicted stress–strain curve can be modified by adjusting the parameters N and C^R; however, the patterns of the texture are insensitive to those parameters. In any event, in accord with experimental observations, the predicted locking strain in tension is far less than in compression, and terminal strain hardening is much steeper. The clean separation of the stress–strain behaviour of the tension and plane strain compression behaviour from those in uniaxial compression and simple shear is a direct demonstration of the difference between *convergent* and *divergent* flow behaviour mentioned.

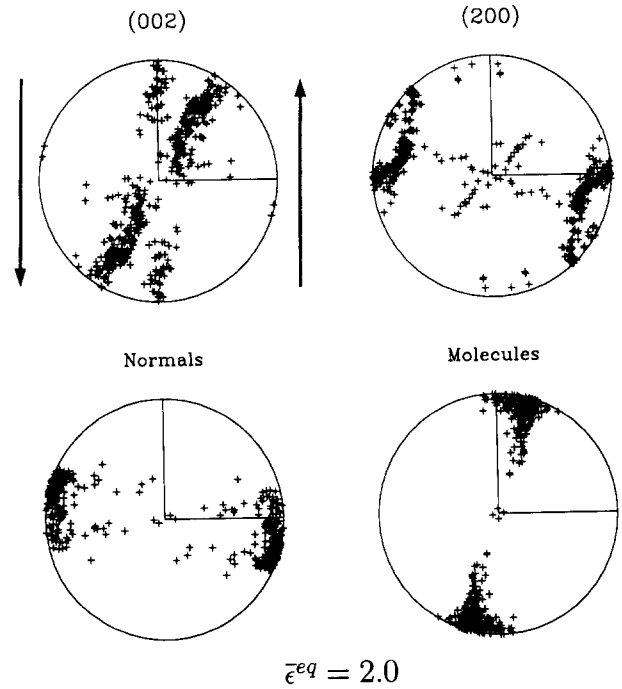

Figure 15 Predicted crystallographic textures, morphological texture and the amorphous phase molecular alignment for HDPE subject to simple shear at $\bar{\varepsilon}^{eq} = 2.0$

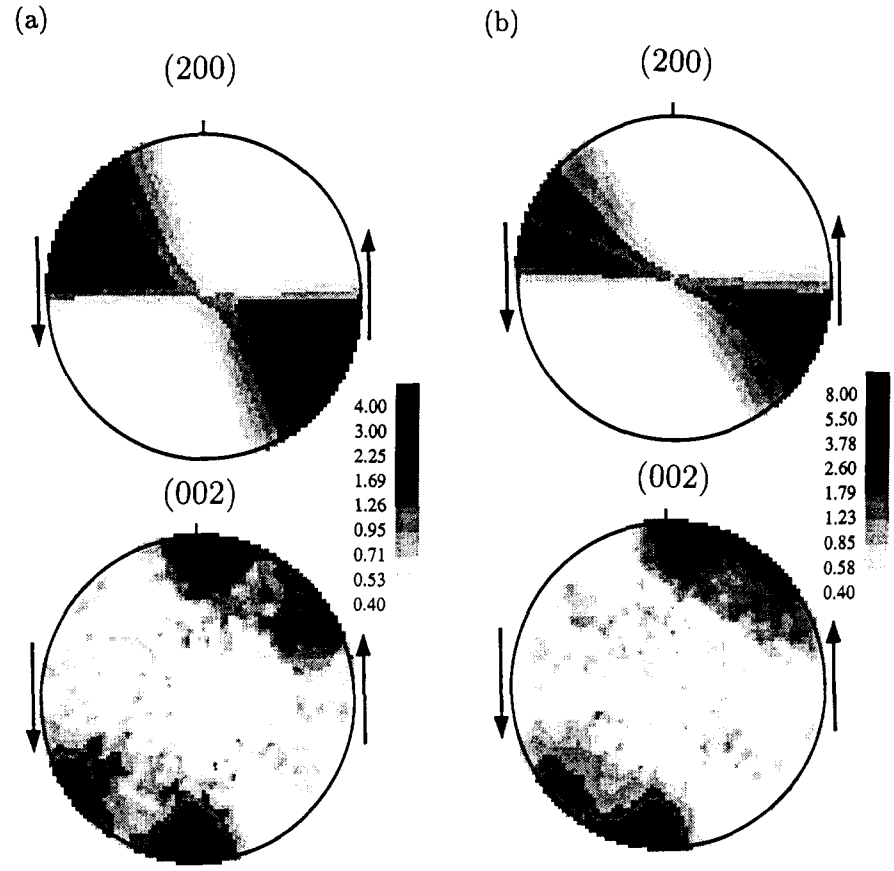

Figure 16 Plots of the WAXS intensities of the diffraction by (200) and (002) planes of HDPE subject to simple shear for: (a) $\bar{\gamma}=1.8$; (b) $\bar{\gamma}=3.0$ (see ref. 10)

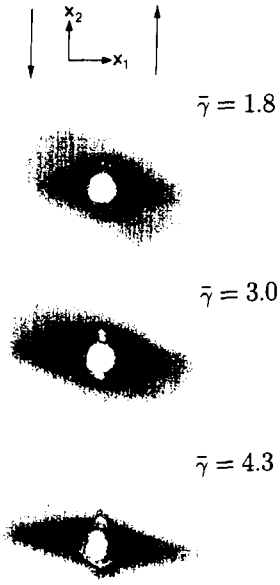

Figure 17 Plots of SAXS patterns viewed from the neutral direction (or x_3-axis) for simple shears $\bar{\gamma}$ of magnitudes 1.8, 3.0 and 4.3 (see ref. 10)

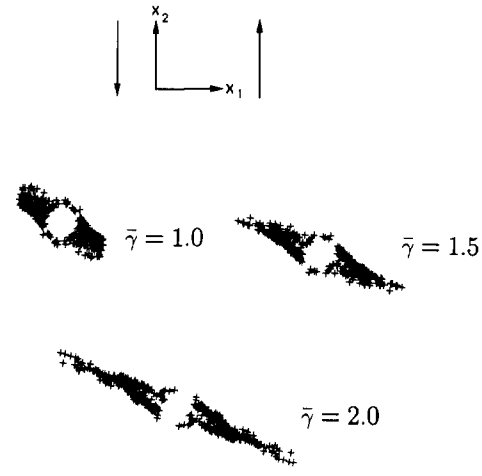

Figure 18 Plots of numerically constructed SAXS patterns viewed from the neutral direction (or x_3-axis) for simple shears $\bar{\gamma}$ of magnitudes 1.0, 1.5 and 2.0

Figures 19 and *20* show the predicted textures at $\bar{\varepsilon}^{eq}=0.8$ and 1.3. In each pole figure, the axis perpendicular to the projection plane is the tensile direction. As the remote strain increases, the pole of the (002) planes rotates toward the tensile direction, and the (200) texture tends toward a circumferentially uniform one near the radial direction. The lamellar normals point predominantly in the radial direction, while the amorphous phase direction of maximum stretch aligns with the macroscopic extension direction.

For macroscopic tensile loading, the normalized equivalent volume-averaged strain rate and stress of each domain are plotted in *Figure 21 versus* $\bar{\varepsilon}^{eq}$. Referring to the crystallographic textures shown in *Figures 19* and *20*, we conclude that initially, the competition of macroscopic deformation accommodation via chain slip and amorphous domain shearing does not allow the chain axes to align fully with the tensile direction for small strain. However, at large strain, after the amorphous phase begins to lock,

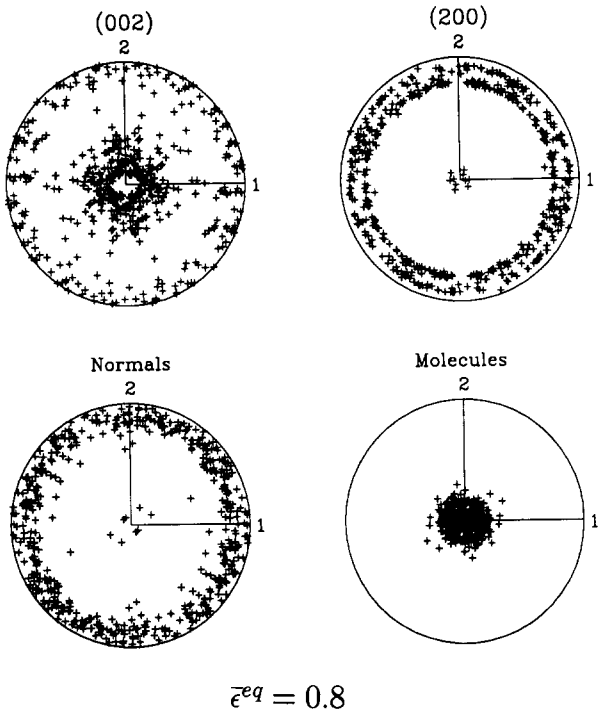

Figure 19 Predicted crystallographic textures, morphological texture (lamellae normals) and the amorphous phase molecular alignment for HDPE subject to uniaxial tension at $\bar{\varepsilon}^{eq} = 0.8$. (Tensile direction is along the 3-axis)

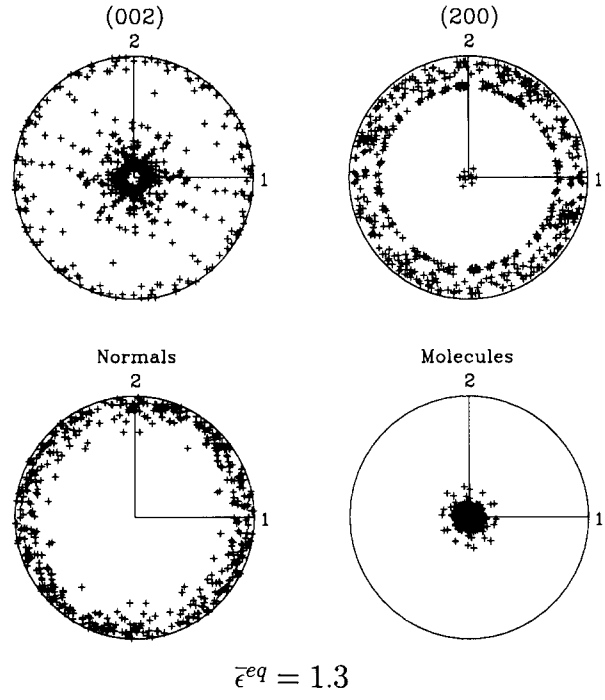

Figure 20 Predicted crystallographic textures, morphological texture and the amorphous phase molecular alignment for HDPE subject to uniaxial tension at $\bar{\varepsilon}^{eq} = 1.3$. (Tensile direction is along the 3-axis)

deformation is transferred principally to the crystalline regions, where chain slip sharpens the texture.

The numerically constructed SAXS patterns as viewed from the radial direction are shown in *Figure 22* for macroscopic strains of 0.4, 0.8 and 1.2. As strain increases, the SAXS patterns change from a uniform ring pattern to a four-point pattern oriented in the radial direction. This implies that the lamellae tend to align with the tensile direction, with their normals rotating toward the radial direction. However, they are prevented from reaching their goal by some of the lamellae undergoing chain slip. The mean thickness of deformed lamellae decreases while the variation in thickness increases. Some of the few lamellae whose normals remain near the loading direction tend to thicken, however. This expected SAXS patterns evolution presupposes no long period restructuring, which has been observed at large plane strain compression[11] and should also occur in the mechanically equivalent plane strain tension. We discuss this point further in the next section and in the Discussion section.

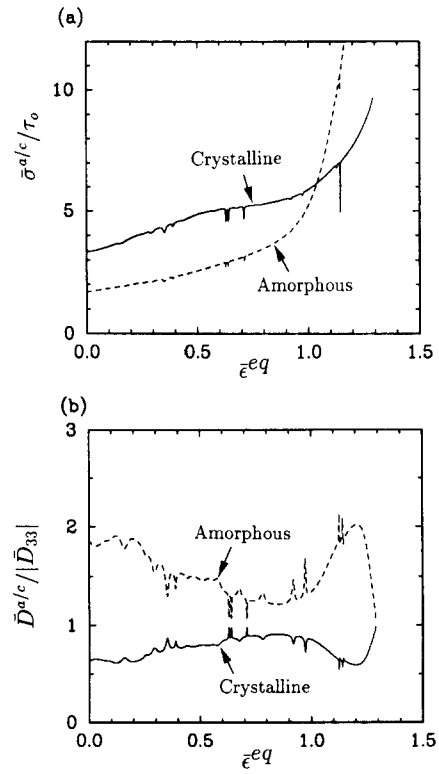

Figure 21 (a) Equivalent phase-volume-averaged stress normalized by τ_0, in both phases, as functions of $\bar{\varepsilon}^{eq}$; (b) equivalent phase-volume-averaged strain rate normalized by the applied macroscopic strain rate, in both phases, as functions of $\bar{\varepsilon}^{eq}$ for uniaxial tension

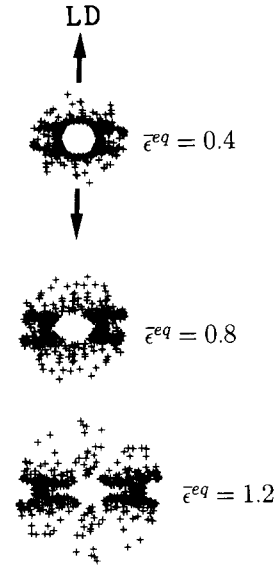

Figure 22 Plots of numerically constructed SAXS patterns viewed from a radial direction for $\bar{\varepsilon}^{eq}$ of 0.4, 0.8 and 1.2 in uniaxial tension

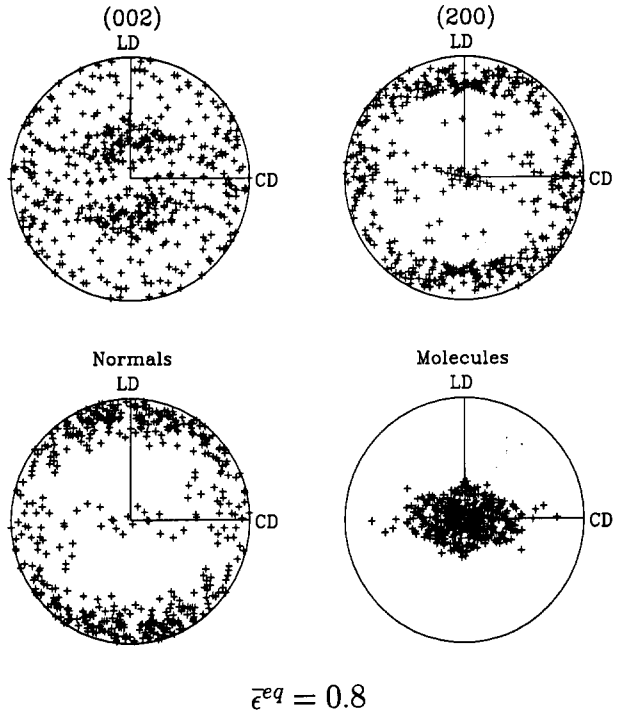

Figure 23 Predicted crystallographic textures, morphological texture (lamellae normals) and the amorphous phase molecular alignment for HDPE subject to plane strain compression at $\bar{\varepsilon}^{eq} = 0.8$. (Flow direction is along the 3-axis)

Due to the known profusion of both local (cavitation) and global (necking) deformation instabilities that afflict the tension test, we did not perform serious experiments on HDPE in uniaxial tension. However, comparing predicted crystallographic textures with experimental results obtained by Krause and Hosford[38], a reasonable agreement is obtained for the crystallographic textures. Experimental observations[38] also confirm that as strain increases, the cluster of chain axes gradually rotates toward the tension direction, as shown in *Figures 19* and *20*. We note in passing that by using axisymmetric extrusion, cavitation should be suppressed, with only minor changes in resulting texture, as compared to uniaxial tension, and is a suggested mode for further experimental study of tensile flow.

Plane strain compression

A final test consists of simulating plane strain compression as it develops in a channel-die of HDPE. The channel-die compression experiment was performed by Galeski *et al.*[11] at a temperature of 80°C. In order to compare properly with the experimental observations, the (common) strain-rate sensitivity exponent n, the relative resistance of the slip systems in the crystalline phase of HDPE and the material constants in the amorphous phase (a, N and C^R) should be chosen accordingly. Due to insufficient experimental information on HDPE at different temperatures, the same set of material constants used in the previous tests is employed to simulate the constant strain rate plane strain compression test of HDPE.

Our prediction of $\bar{\sigma}^{eq}$ *versus* $\bar{\varepsilon}^{eq}$ at room temperature is included in *Figure 6* (with $\bar{D}^{eq}/\dot{\gamma}_0 = 1$). Texture evolution is shown in *Figures 23* and *24* for $\bar{\varepsilon}^{eq} = 0.8$ and 1.3, respectively. In each pole figure, the direction perpendicular to the projection plane is the flow direction. The loading direction and the constraint direction are denoted by LD and CD, respectively. In these figures there is a monotonic migration of the (200) poles toward the loading direction and a corresponding monotonic migration of the (002) poles toward the flow direction. In both cases, however, full alignment is stifled, never quite reaching the geometrical goals. The orientations of directions of maximum stretch in the amorphous phase show strong alignment in the flow direction. As in the previous cases of uniaxial tension/compression and simple shear, the lamellar normals and the chain axes rotate in opposite directions. The simulations predict a monotonic migration of the lamellar normals toward the loading direction.

The numerically constructed SAXS patterns at equivalent macroscopic strain levels of 0.4, 0.8 and 1.2, as viewed from the constraint direction (the neutral direction for plane strain compression) and the flow direction are shown in *Figures 25a* and *b*, respectively. As strain increases, the predicted SAXS patterns viewed from the constraint direction change progressively from a uniform ring pattern to a four-point pattern, while those viewed from the flow direction develop a two-point pattern. At large strain, the SAXS patterns viewed from both directions predict that the lamellar normals rotate toward the loading direction, with decreasing lamellar thickness.

Plane strain compression and uniaxial tension belong to a class of macroscopically irrotational large strain deformations which differ quite significantly in their consequences from uniaxial compression and simple shear. To highlight these differences we compare here the predictions of our simulation of channel-die compression with the experimental results of Galeski *et al.*[11]. *Figures 26a* and *27a* show experimental pole figure patterns of the (002) and (200) planes at $\bar{\varepsilon}^{eq} = 0.92$ and 1.86, respectively. The orientations of normals to segments of

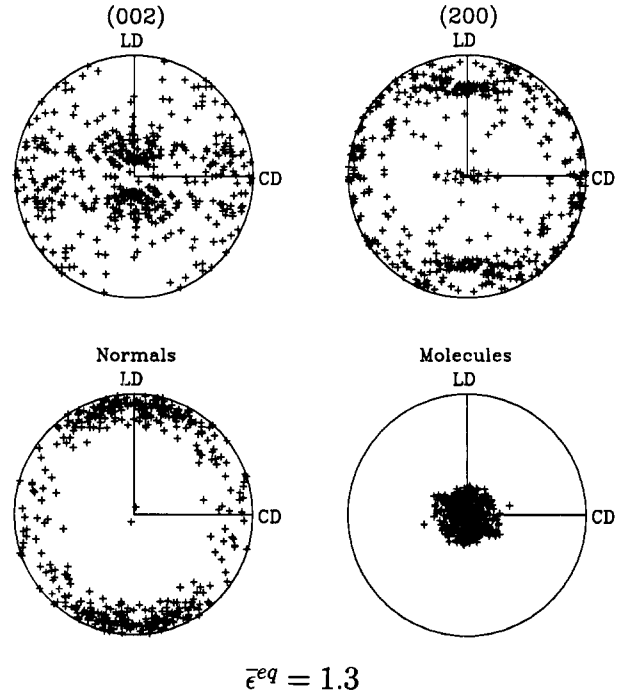

Figure 24 Predicted crystallographic textures, morphological texture and the amorphous phase molecular alignment for HDPE subject to plane strain compression at $\bar{\varepsilon}^{eq} = 1.3$. (Flow direction is along the 3-axis)

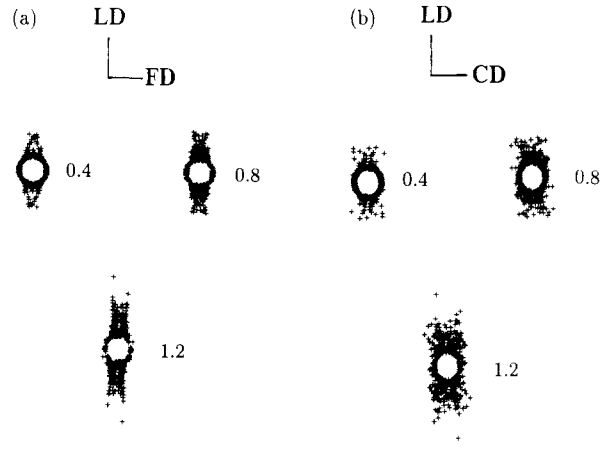

Figure 25 Plots of numerically constructed SAXS patterns viewed from (a) the constraint direction and (b) the flow direction for $\bar{\varepsilon}^{eq}$ of 0.4, 0.8 and 1.2 in plane strain compression

macromolecular chain in the amorphous domain obtained from an X-ray peak deconvolution process discussed in detail by Galeski *et al.*[11] are shown in *Figures 26b* and *27b*. In these figures, the view is from the flow direction. Information on the clustering of the lamellar normals is given in *Figure 28* in the form of the associated SAXS patterns viewing the deformed material from the constraint direction and the flow direction, respectively, for four equivalent strain levels of 0.44, 0.92, 1.15 and 1.86.

In *Figure 26a*, for $\bar{\varepsilon}^{eq}=0.92$, the (200) poles have distinctly rotated toward the loading direction and the (002) poles have rotated toward the flow direction. Both of these rotations have reached a position roughly 20° from their ultimate target, very much like the trend shown in the simulation results of *Figures 23* and *24*. In *Figure 27a*, at $\bar{\varepsilon}^{eq}=1.86$, a high degree of crystallographic orientation is obtained, producing a texture resembling a monocrystal, with (002) poles oriented in the flow direction and (200) poles oriented in the loading direction. Moreover, from *Figures 26b* and *27b*, the orientation of the normals to macromolecular chain segments in the amorphous regions rotate perpendicular to the flow direction and thus the chains in the amorphous phase form an orientation parallel to the flow direction. This is in good agreement with the simulation results shown in *Figures 23* and *24*.

The experimental SAXS patterns in *Figure 28* for $\bar{\varepsilon}^{eq}=0.44$, 0.92 and 1.15 show that the lamellar normals have very discernibly begun to cluster around the loading direction, as predicted in *Figure 25* (also *Figures 23* and *24*). The progressive thinning of the lamellae is also confirmed by the SAXS patterns. In *Figure 28a*, the SAXS patterns viewed from the constraint direction show a continuous change from a uniform ring into an elongated elliptic shape with a visible four-point pattern. On the other hand, the SAXS patterns viewed from the flow direction change continuously from a uniform ring into an elongated ellipse with practically a two-point pattern. These features are qualitatively in excellent agreement with the simulation results of *Figure 25*.

The SAXS patterns in *Figure 28a* show that beyond $\bar{\varepsilon}^{eq}=1.15$, some new events begin to occur. The clear clustering of the lamellar normals has distinctly bifurcated away from the loading direction and toward the flow direction. As $\bar{\varepsilon}^{eq}$ is increased to 1.86, the four-point pattern viewed from the constraint direction transforms into two arcs normal to the flow direction. The two-point pattern viewed from the flow direction, shown in *Figure 28b*, is now much better outlined. These data indicate that the lamellae were oriented first preferentially perpendicular to the loading direction, as predicted by the model, and then, for $\bar{\varepsilon}^{eq}>1.15$, the SAXS patterns viewed from the flow direction become progressively fainter, showing a gradual elimination of those lamellae previously oriented with their normals parallel to the loading direction. The SAXS pattern for $\bar{\varepsilon}^{eq}=1.86$ in *Figure 28a* shows evidence for restructuring of a new set of lamellae and amorphous regions, i.e. a new long period. Thus the lamellar normals in the final, fully textured material are nearly parallel with the flow direction, or the direction of principal molecular alignment. The formation of these new lamellae, as a major morphological restructuring process, had not been fully elucidated until recently[11]. Galeski *et al.*[11] proposed a scenario based on their TEM observations and the SAXS results to explain how this newly evolving amorphous material may be topologically related to the initial amorphous material. These restructuring processes were not incorporated into the current model, thus limiting the predictions to deformation to equivalent strains less than the experimentally observed onset of restructuring. However, the predictions are in very good agreement with the experiments up to that point.

DISCUSSION

Development of deformation induced texture in semi-crystalline polymers resulting in large stiffness and strength anisotropies has been known for decades (for reviews see refs 40 and 41). The technological importance of these phenomena in applications involving production of high modulus fibres and ribbons and precursors for high modulus carbon fibre is widely appreciated. In view of this importance there has been intense experimental research activity since the late 1960s and early 1970s in the study of the mechanisms of the morphological alterations that produce the texture (for a review see ref. 42). With few exceptions[43,44], this early research relied heavily on the uniaxial tension experiment and a multitude of imaginative micro-experiments carried out on electron transparent thin films, studied by means of TEM. These experiments have produced a bewildering collection of deformation features. Many of these experiments have been invaluable in clarifying the crystal structure and forms of crystallization of long chain polymers, as well as how these chain molecular lamellar crystals are associated with a ubiquitous amorphous phase. On the other hand, they were instrumental in establishing a distorted picture of how the deformation evolved and resulted in texture. Since most investigations concentrated on the details of the tension experiment, which undergoes a variety of inessential and often confusing deformation instabilities, it was believed that large strain texture development necessitated a stage of release of interlamellar constraints by cavitation, which then permitted the unravelling of lamellae followed by unhindered chain alignment, in a process referred to as micronecking[39]. The early rolling experiments of Keller and Pope[43] and channel-die compression experiments of Young and Bowden[44] and the much more detailed recent experiments of Galeski *et al.*[11], also in plane strain

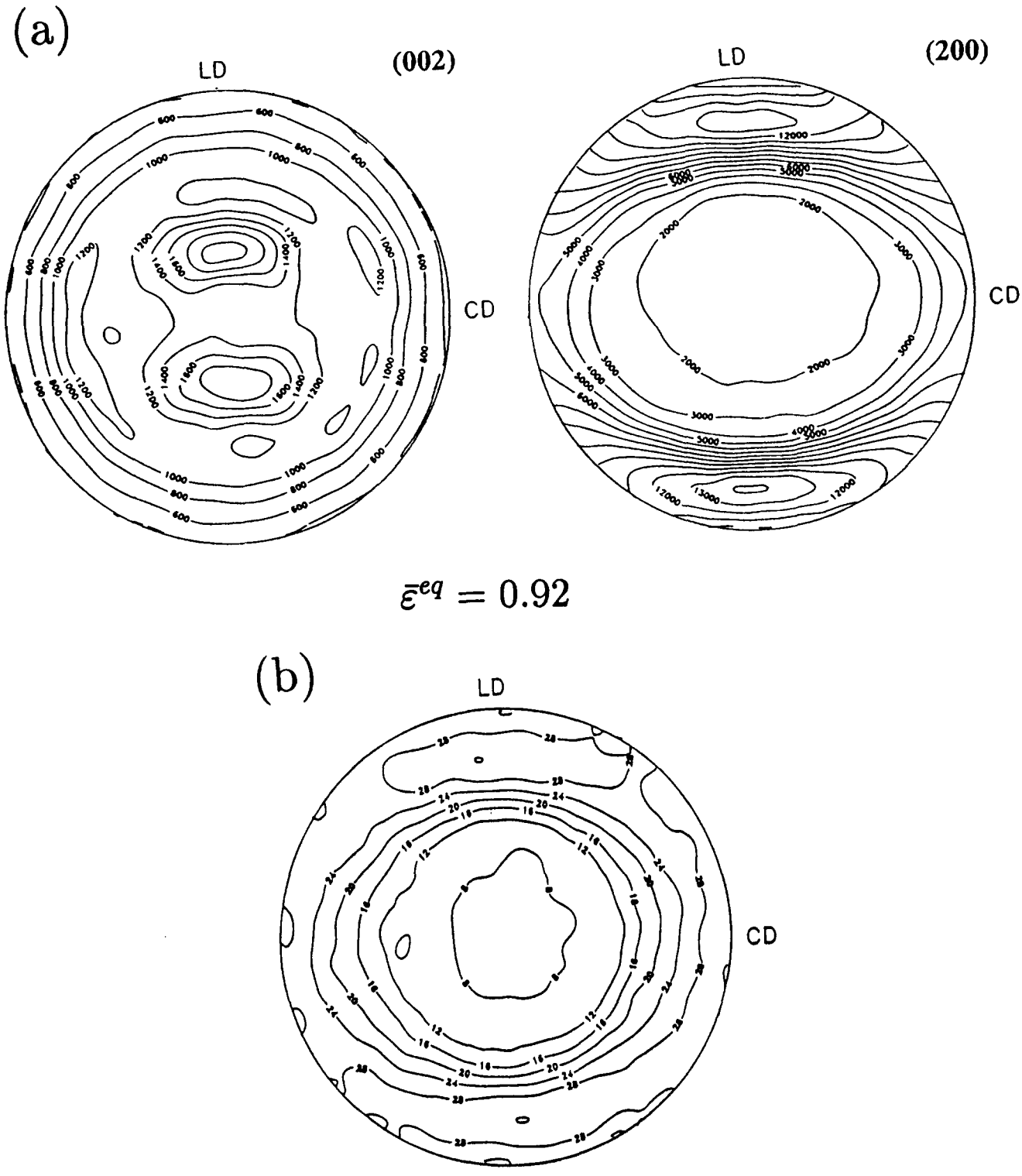

Figure 26 Plots of (a) the WAXS intensities of the diffraction by (002) and (200) planes and (b) the orientation of normals to segments of macromolecular chains in the amorphous region obtained from an X-ray peak deconvolution process of HDPE subjected to plane strain compression at $\bar{\varepsilon}^{eq} = 0.92$ (see ref. 11)

compression, have all demonstrated that the same very high degree of texture evolution, molecular alignment and long-period restructuring occurs in large strain compression flow as in uniaxial tension — but without the cavitation or so-called micronecking stage. How this occurs quite naturally in the course of large strain extensional flow through eventual repeated pinch-off in the stretched lamellae has been discussed in detail with ample TEM, WAXS and SAXS evidence[11]. This emerging mechanistic understanding has established the point of view that development of deformation induced texture in semicrystalline polymers can be described by a continuous succession of volume preserving shear transformations occurring in the crystalline lamellae and the associated amorphous layers compatibly. This is the approach which we have developed in a series of computational models[14,21,31,32] for HDPE, in association with our experimental studies of this phenomenon[6,8,10,11] in this material. In this paper we have compared the results of this computer simulation

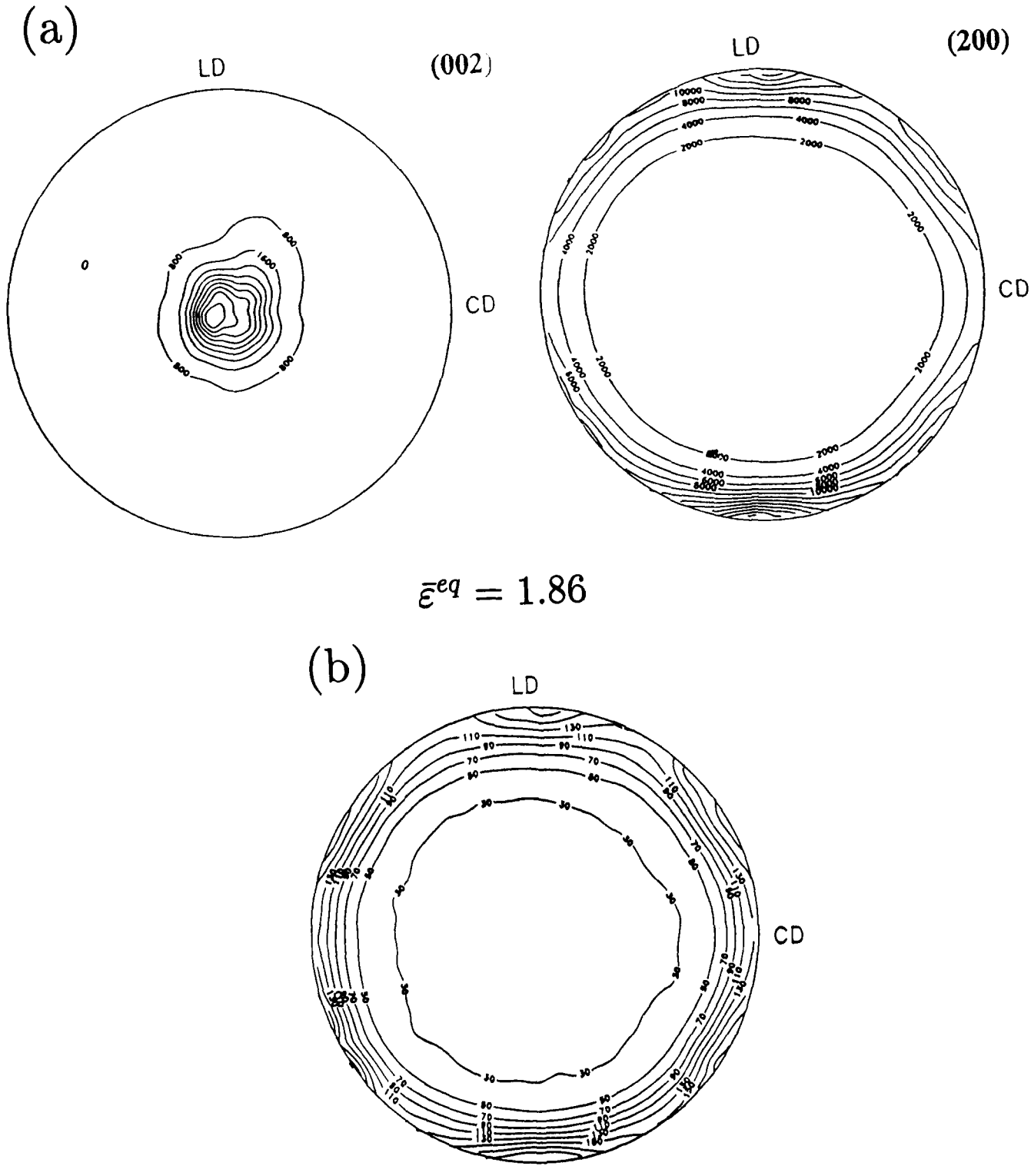

Figure 27 Plots of (a) the WAXS intensities of the diffraction by (002) and (200) planes and (b) the orientation of normals to segments of macromolecular chains in the amorphous region obtained from an X-ray peak deconvolution process of HDPE subjected to plane strain compression at $\bar{\varepsilon}^{eq} = 1.86$ (see ref. 11)

with these experimental results. While the present computer simulation has been specifically tailored to the orthorhombic crystal structure of HDPE, the developed methodology can be readily adapted to the corresponding deformation induced texturing of monoclinic Nylon 6[45] and triclinic PET[46], and any other semicrystalline aggregation, the initial morphology and the deformation mechanisms of which can be definitively stated as initial conditions and constitutive behaviour given.

As we have demonstrated above, our computer model has a high degree of precision in the simulation of both the evolving plastic resistances and deformation induced textures in the 'divergent' flow modes of straining of uniaxial compression and simple shear where no long period restructuring by lamellar pinch-off has been observed. In the case of plane strain compression by means of channel-die extrusion, our simulation is able to follow the evolution of texture in all respects up to the occurrence of the long period restructuring at an equivalent strain of > 1.15. Above this critical strain our

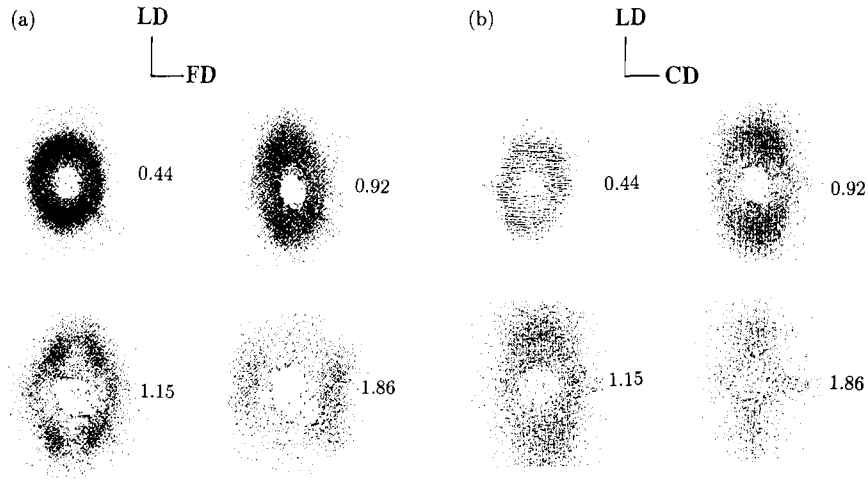

Figure 28 Plots of SAXS patterns viewing the material from (a) the constraint direction and (b) the flow direction for $\bar{\varepsilon}^{eq}$ of 0.44, 0.92, 1.15 and 1.86 in plane strain compression (see ref. 11)

simulation is still able to predict the crystallographic texture correctly, but does not predict the further evolution of the lamellar morphology, since apparently this involves lamella pinch-off and extensive interface migration to reduce stored interfacial free energy. Such processes could be simulated separately but this has not yet been done.

Simulation of deformation textures in polycrystalline face centred cubic and body centred cubic metals has been done by numerous investigators since Sachs[27] and Taylor[28] pointed out the basic geometrical and operational requirements (for a recent example see ref. 47). In these simulations, in all cases, the Taylor requirements of availability of five independent slip systems is always satisfied, and there are no important kinematical constraints that need to be dealt with. In semicrystalline polymers with molecular chain crystalline lamellae, this requirement is not satisfied because of the relative inextensibility of the lamellae in the chain direction. Thus, in the deformation of lamellar aggregates, those lamellae which are in orientations where they need to respond by straining in the chain direction, will act as rigid inclusions. This severe constraint causes the usual Taylor-type models based on an affine connection between the local and global flow fields to break down. To cope with this constraint we have developed special operational approaches for both Taylor-type models[21,31,32] and Sachs-type models[14], which amount to the introduction of local hybrid procedures to overcome the problem.

CONCLUSIONS

We employed a newly developed micromechanically based composite model[14] to study plastic deformation and texture evolution in initially isotropic HDPE subject to uniaxial tension and compression, simple shear and plane strain compression. The predicted results agree with the experimental observations of macroscopic stress–strain behaviour and texture evolution in nearly all aspects. In the case of channel-die compression, the predicted morphological texture for large strain was in some contradiction with existing experimental results. The contradiction arises from a long period restructuring process that appears in large strain extensional flow due to extensive lamellae pinch-off. This process, which has been studied in detail by us and reported elsewhere[11], has not been incorporated into the present simulation. Nevertheless, our model, even lacking this restructuring, has sharpened the focus on the complex processes of texture development. The present micromechanically based composite model can also be applied to study plastic deformation and texture evolution in other initially isotropic semicrystalline polymers, e.g. PET and Nylon 6, as well as in initially oriented semicrystalline polymers.

ACKNOWLEDGEMENTS

This work was supported by a DARPA U.R.I. programme under ONR Contract no. N00014-86-K-0768. We are pleased to acknowledge useful discussions with Professors R. E. Cohen and C. G'Sell and Dr A. Galeski.

REFERENCES

1 Frank, F. C., Keller, A. and O'Connor, A. *Phil. Mag.* 1958, **3**, 64
2 Seto, T., Hara, T. and Tanaka, T. *Jpn J. Appl. Phys.* 1968, **7**, 31
3 Young, R. J., Bowden, P. B., Richie, J. and Rider, J. G. *J. Mater. Sci.* 1973, **8**, 23
4 Bowden, P. B. and Young, R. J. *J. Mater. Sci.* 1974, **9**, 2034
5 Haudin, J. M. in 'Plastic Deformation of Amorphous and Semi-Crystalline Materials' (Eds B. Escaig and C. G'Sell), Les Editions de Physique, Les Ulis, 1982, p. 291
6 Bartczak, Z., Argon, A. S. and Cohen, R. E. *Macromolecules* 1992, **25**, 5036
7 G'Sell, C. and Jonas, J. J. *J. Mater. Sci.* 1979, **14**, 583
8 Bartczak, Z., Cohen, R. E. and Argon, A. S. *Macromolecules* 1992, **25**, 4692
9 G'Sell, C., Boni, S. and Shrivastava, S. *J. Mater. Sci.* 1983, **18**, 903
10 Bartczak, Z., Argon, A. S. and Cohen, R. E. *Polymer* in press
11 Galeski, A., Bartczak, Z., Argon, A. S. and Cohen, R. E. *Macromolecules* 1992, **25**, 5705
12 Khoury, F. and Passaglia, E. in 'Treatise on Solid State Chemistry' (Ed. N. B. Hannay), Vol. 3, Plenum Press, New York, 1976, p. 335
13 Hoffman, J. D., Davis, G. T. and Lauritzen, J. I. in 'Treatise on Solid State Chemistry', (Ed. N. B. Hannay), Vol. 3, Plenum Press, New York, 1976, p. 497
14 Lee, B. J., Parks, D. M. and Ahzi, S. *J. Mech. Phys. Solids* submitted
15 Lin, L. PhD Dissertation, Massachusetts Institute of Technology, 1991

16 Pope, D. P. and Keller, A. *J. Polym. Sci., Polym. Phys. Edn* 1975, **13**, 533
17 Burney, G. S. and Groves, G. W. *J. Mater. Sci.* 1978, **13**, 639
18 Hutchinson, J. W. *Proc. R. Soc. (London) A* 1976, **348**, 101
19 Pan, J. and Rice, J. R. *Int. J. Solids Struct.* 1983, **19**, 973
20 Asaro, R. J. and Needleman, A. *Acta Metall.* 1985, **33**, 923
21 Parks, D. M. and Ahzi, S. *J. Mech. Phys. Solids* 1990, **38**, 701
22 Haward, R. N. and Thackray, G. *Proc. R. Soc. (London) A* 1968, **302**, 453
23 Argon, A. S. *Phil. Mag.* 1973, **28**, 39
24 Mott, P. H., Argon, A. S. and Suter, U. W. *Phil. Mag.* 1993, **67**, 931
25 Boyce, M. C., Parks, D. M. and Argon, A. S. *Mech. Mater.* 1988, **7**, 15
26 Arruda, E. M. and Boyce, M. C. *J. Mech. Phys. Solids* 1993, **41**, 389
27 Sachs, G. *Z. Verein Duet. Ing.* 1928, **72**, 734
28 Taylor, G. I. *J. Inst. Metals* 1938, **62**, 307
29 Molinari, A., Canova, G. R. and Ahzi, S. *Acta Metall.* 1987, **35**, 2983
30 Eshelby, J. D. *Proc. R. Soc. (London) A* 1957, **241**, 376
31 Ahzi, S., Parks, D. M. and Argon, A. S. in 'Computer Modeling and Simulation of Manufacturing Processes' (Eds. B. Singh *et al.*), ASME, New York, 1980, p. 287
32 Parks, D. M. and Ahzi, S. in 'IUTAM Symposium on Inelastic Behavior of Composite Materials' (Ed. G. J. Dvorak), Springer-Verlag, New York, 1990, p. 325
33 Hill, R. *Proc. R. Soc. (London) A* 1972, **326**, 131
34 Keller, A. and Sawada, S. *Macromol. Chem.* 1964, **74**, 190
35 Bassett, D. C. and Hodge, A. M. *Proc. R. Soc. (London) A* 1981, **377**, 25
36 Varnell, W. D., Ryba, E. and Harrison, I. R. *J. Macromol. Sci. Phys.* 1987, **B26**, 135
37 G'Sell, C. and Dahoun, A. to be published
38 Krause, S. J. and Hosford, W. F. *J. Polym. Sci., Polym. Phys. Edn* 1989, **27**, 1853
39 Peterlin, A. *J. Mater. Sci.* 1971, **6**, 490
40 Ward, I. M. (Ed.) 'Structure and Properties of Oriented Polymers', Halsted Press, New York, 1975
41 Ciferri, A. and Ward, I. M. (Eds) 'Ultra-High Modulus Polymers', Applied Science, London, 1979
42 Lin, L. and Argon, A. S. *J. Mater. Sci.* in press
43 Keller, A. and Pope, D. P. *J. Mater. Sci.* 1971, **6**, 453
44 Young, R. J. and Bowden, P. B. *Phil. Mag.* 1974, **29**, 1061
45 Lin, L. and Argon, A. S. *Macromolecules* 1992, **25**, 4011
46 Bellare, A., Cohen, R. E. and Argon, A. S. *Polymer* 1993, **34**, 1393
47 Kalidindi, S. R., Bronkhorst, C. A. and Anand, L. *J. Mech. Phys. Solids* 1992, **40**, 537